

Radical Intermediates in the Addition of OH to Propene: Photolytic Precursors and Angular Momentum Effects

M. D. Brynteson,[†] C. C. Womack,[†] R. S. Booth,[†] S.-H. Lee,[‡] J. J. Lin,[§] and L. J. Butler^{†,*}

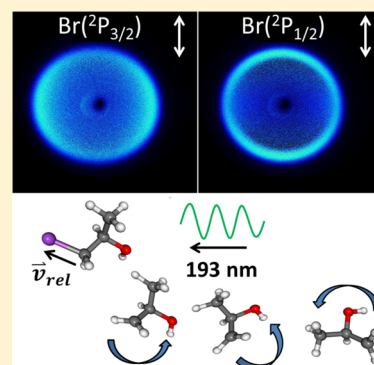
[†]Department of Chemistry and the James Franck Institute, The University of Chicago, Chicago, Illinois 60637, United States

[‡]National Synchrotron Radiation Research Center, Hsinchu 30076, Taiwan, Republic of China

[§]Institute of Atomic and Molecular Sciences, Academia Sinica, Taipei 10617, Taiwan, Republic of China

Supporting Information

ABSTRACT: We investigate the photolytic production of two radical intermediates in the reaction of OH with propene, one from addition of the hydroxyl radical to the terminal carbon and the other from addition to the center carbon. In a collision-free environment, we photodissociate a mixture of 1-bromo-2-propanol and 2-bromo-1-propanol at 193 nm to produce these radical intermediates. The data show two primary photolytic processes occur: C–Br photofission and HBr photoelimination. Using a velocity map imaging apparatus, we measured the speed distribution of the recoiling bromine atoms, yielding the distribution of kinetic energies of the nascent C₃H₆OH radicals + Br. Resolving the velocity distributions of Br(²P_{1/2}) and Br(²P_{3/2}) separately with 2 + 1 REMPI allows us to determine the total (vibrational + rotational) internal energy distribution in the nascent radicals. Using an impulsive model to estimate the rotational energy imparted to the nascent C₃H₆OH radicals, we predict the percentage of radicals having vibrational energy above and below the lowest dissociation barrier, that to OH + propene; it accurately predicts the measured velocity distribution of the stable C₃H₆OH radicals. In addition, we use photofragment translational spectroscopy to detect several dissociation products of the unstable C₃H₆OH radicals: OH + propene, methyl + acetaldehyde, and ethyl + formaldehyde. We also use the angular momenta of the unstable radicals and the tensor of inertia of each to predict the recoil kinetic energy and angular distributions when they dissociate to OH + propene; the prediction gives an excellent fit to the data.



INTRODUCTION

The oxidation of unsaturated hydrocarbons by the hydroxyl radical is an important reaction in both atmospheric and combustion chemistry. Our experiment focuses on the reaction of OH with propene, a simple unsaturated hydrocarbon with two sites at which addition of the OH may occur. To date, many studies on the reaction rate over a wide range of temperatures have been performed on this system, both experimental^{1–31} and theoretical.^{32–34} These studies have shown that the addition of OH to propene dominates at temperatures below 500 K. Beyond 500 K, hydrogen abstraction becomes an important part of the mechanism and begins to dominate at much higher temperatures. In addition, ethene and propene flame studies have given evidence for the presence of enols, which has increased interest in the product branching resulting from OH-initiated oxidation.^{35,36}

The addition of the hydroxyl radical to propene offers a wider variety of products than the addition of OH to ethene as the addition to propene may occur via two pathways: addition to the terminal carbon and addition to the center carbon. Experimental results show the branching between the center and terminal carbon addition favors the terminal carbon, with approximately 65–75% of additions leading to terminal carbon addition.^{37–39} Theory has given similar results, yielding predictions of ~65% of additions to the terminal carbon.^{40,41}

In our study of the reaction between OH and propene, we directly generate the radical intermediates formed upon addition of the hydroxyl radical by photodissociating two halogenated precursors. Using 193 nm radiation, photolysis of a mixture of 2-bromo-1-propanol and 1-bromo-2-propanol results in C–Br bond fission, yielding the radical intermediates of interest. These intermediates are formed in a collision-free environment with a range of vibrational and rotational energies. This results in a portion of radical intermediates stable to further dissociation and a portion having enough energy to surmount various barriers to dissociation, the lowest of which is the barrier to OH and propene.

We present results of two predictive models, one for treating the rotational energy in the nascent radicals and one for estimating the energy imparted to relative kinetic energy when the radicals dissociate to OH + propene. The first model is an extension of one used by Ratliff et al.⁴² and Womack et al.,⁴³ which is used to predict the rotational energy imparted to the nascent radicals from the C–Br photofission. As in the prior work, the model uses the measured recoil kinetic energy distribution and the geometry of the precursor in the Franck–Condon

Received: November 5, 2013

Revised: March 6, 2014

Published: April 23, 2014

region of the repulsive excited state to estimate the distribution of angular momenta in the nascent radicals. We use an extension⁴⁴ of this model that uses the full inertia tensor to correctly account for the change in rotational energy of the nascent radicals as they progress along the dissociation reaction coordinate. This allows us to predict which radicals have enough internal energy at the centrifugally corrected transition state to dissociate to OH + propene and which radicals do not. The second model, developed herein, builds on the previous model and uses the angular momentum in the radicals to predict the resulting speed and angular distributions of the OH and propene fragments. These models are shown to be in good agreement with experimental results and yield useful information about the energy partitioned between rotation and vibration in the radicals generated by our photolysis method and the energy partitioned to relative kinetic energy when those nascent radicals dissociate.

In addition to our characterization of the above energy partitioning, we present evidence for three of the radicals' dissociation channels: OH + propene, methyl + acetaldehyde, and ethyl + formaldehyde. The calculated barrier heights to these dissociation channels suggest they are the most likely, and our time-of-flight spectra and speed distributions of these fragments evidence momentum-matched products for each of these dissociation channels. Our spectra also evidence close-to-symmetric forward-backward scattering which indicates the rotational period of the radical intermediates is much shorter than their lifetime.

■ EXPERIMENTAL METHODS

1. Velocity Map Imaging. This work uses a 2-D velocity map imaging apparatus, described previously,^{45–48} to detect the speed distributions of Br atoms, $m/z = 42$ fragments, and $m/z = 31$ fragments. A supersonic beam of the 70/30 mixture of 1-bromo-2-propanol and 2-bromo-1-propanol was created by seeding the vapor pressure of the liquid sample (~ 7 Torr) in He to a concentration of $\sim 1.4\%$. (The individual brominated isomers are not commercially available in pure form, nor can the 70/30 mixture be separated with distillation.) At a total stagnation pressure of 500 Torr, the molecular beam was supersonically expanded through a heated General Valve Iota One pulsed valve with an orifice diameter of 0.8 mm and a temperature of 80 °C.

After passing through a skimmer, the molecular beam crossed, at right angles, the polarized 193.3 nm photodissociation light from a GAM (EX10F/300) ArF laser. We use the vertically polarized component obtained by passing the unpolarized 193.3 nm output of the laser through a single crystal quartz birefringent Pellin-Broca. A lens focused the vertically polarized beam to a focal point approximately 4 mm after its intersection with the molecular beam.

The photolysis laser is fired 40 ns prior to the ionization laser. Two ionization schemes were used in detection of the recoiling fragments. For the bromine atoms, we used 2 + 1 resonance-enhanced multiphoton ionization (REMPI) to state-selectively ionize the $\text{Br}(^2\text{P}_{3/2})$ and $\text{Br}(^2\text{P}_{1/2})$ photofragments with 233.681 nm ($5p\ ^4\text{P}_{1/2} \leftarrow 4p\ ^2\text{P}_{3/2}$) and 234.021 nm ($5p\ ^2\text{S}_{1/2} \leftarrow 4p\ ^2\text{P}_{1/2}$) photons, respectively. Tripling the output of a Lambda Physik FL 3002 dye laser (LDS 698 dye) pumped by an Nd:YAG laser (Continuum Powerlite Precision 9020) generated these REMPI wavelengths. The ~ 702 nm dye laser output passed through a potassium dihydrogen phosphate crystal, doubling the frequency, and then it was mixed with the

fundamental in a β -barium borate crystal to produce vertically polarized photons at the REMPI wavelength. After focusing with a 25.4 cm focusing lens, this light crossed the molecular beam at a right angle in the main chamber of the imaging apparatus. We determine the spin-orbit branching ratio, $N[\text{Br}(^2\text{P}_{1/2})]/N[\text{Br}(^2\text{P}_{3/2})]$, by integrating the total ion signal from Br atoms in each spin-orbit state, $S[\text{Br}(^2\text{P}_{1/2})]$ and $S[\text{Br}(^2\text{P}_{3/2})]$, in images accumulated while scanning the Doppler profiles ± 0.008 nm from line center and weighting this result by the experimental REMPI line strength, $k = 0.32 \pm 0.02$,⁴² as shown in eq 1. The experimental conditions for REMPI detection of the bromine atoms (i.e., laser power, focal length) were the same as those in ref 42.

$$\frac{N[\text{Br}(^2\text{P}_{1/2})]}{N[\text{Br}(^2\text{P}_{3/2})]} = k \frac{S[\text{Br}(^2\text{P}_{1/2})]}{S[\text{Br}(^2\text{P}_{3/2})]} \quad (1)$$

To detect propene from the major dissociation channel of the $\text{C}_3\text{H}_6\text{OH}$ radicals, we use 10.5 eV ionization generated by tripling the 355 nm output of a pulsed Nd:YAG laser (Continuum Surelite I-20). The 355 nm light passed through a beam expander (focal length = -150 mm and focal length = 300 mm at 588 nm) and then two lenses to focus the light into a 21 cm low-pressure gas cell filled with 22 Torr of high purity Xe ($>99.995\%$). The gas cell, mounted on the main vacuum chamber, ends with a MgF_2 lens (focal length = 120.3 mm at 193 nm) that served as the barrier between the cell and the chamber. This lens recollimated the 355 nm light while focusing the 118 nm light.

Following photodissociation and photoionization, the electrostatic lens optics with repeller and extractor voltages in a ratio of 1.404:1 (2000 and 1424 V for Br atoms and 3932 and 2800 V for the detection of $m/z = 42$ and $m/z = 31$ fragments) accelerated the spherically expanding ions down a ~ 577 mm grounded time-of-flight tube toward the detector. The Burle 3040FM detector is a position sensitive Chevron microchannel plate (MCP) assembly coupled to a P20 phosphor screen. An 80 ns, -750 V pulse on the front plate of the MCP gates the ions based on arrival time. A cooled charge-coupled device (CCD) camera (La Vision Imager 3) with a standard 35 mm lens recorded the images of the ions appearing on the phosphor screen, which remained at 3.3 kV above the potential of the rear MCP plate. We use Houston's ion-counting method⁴⁹ to process the collected images. A digital delay pulse generator (Stanford Research DG535) controlled the timing sequence for opening the pulsed valve, firing the lasers, gating the MCP gain, and capturing the ion images at a repetition rate of 20 Hz.

The images show a burn spot near the center of the detector. The sensitivity of the detector to ions in the area of the burn spot is significantly diminished, but the affected area does not span any farther than 34 pixels from the center of the image. This distance from the center of the image corresponds to speeds of 255 m/s for $m/z = 42$ (C_3H_6^+) fragments, 300 m/s for the $m/z = 31$ fragments, and 134 m/s for the $m/z = 79$ (Br^+) fragments. The measured speed distributions would only be affected in the very low speed tail, far from the bulk of the distribution.

2. NSRRC Scattering Apparatus. The scattering data presented in this paper were taken at the National Synchrotron Radiation Research Center (NSRRC) in Hsinchu, Taiwan, using the U9 Chemical Dynamics Beamline and a crossed laser-molecular beam scattering apparatus. This apparatus has been described in detail elsewhere^{50–52} and only a brief description

will be given here. A supersonic beam of the 70/30 mixture of 1-bromo-2-propanol and 2-bromo-1-propanol was created by seeding the vapor pressure of the liquid sample in neon to a concentration of ~1%. We expanded the gaseous mixture at a stagnation pressure of 600 Torr through a pulsed valve operating at 100 Hz at a temperature of approximately 80 °C. The 193.3 nm output of a LPF 200 Lambda Physik Laser Technik laser, propagating perpendicularly to the plane created by the molecular beam and the detector axis was aligned directly into the chamber. The beam spot measured 3 mm × 3 mm with a pulse width of approximately 15 ns. The output power ranged from 30 to 40 mJ/pulse. Those fragments having the proper net velocity vectors fly through an aperture into the detector and are ionized by the tunable VUV synchrotron radiation at a distance of 10.05 cm from the crossing point of the molecular beam and photodissociation laser. This ionization energy was varied by adjusting the U9 undulator gap. Before entering the detector, the ionization beam passed through a gas filter of ~10 Torr Ar to eliminate the higher harmonics. The ions were then focused and accelerated by voltage plates into an Extrel 1.2 MHz quadrupole, where they were filtered by mass and counted using a Daly detector. A multichannel scalar counted the signal, which is proportional to the number of ions, and that signal was recorded as a function of time-of-flight, the time from the interaction of the molecular beam with the photolysis laser to the detector. The total time-of-flight is the sum of two components. The first component is the neutral flight time of the fragments from photolysis to ionization, and the second component is the time for the ionized fragment to fly from the ionizer through the quadrupole to the Daly detector. The second portion of the total time-of-flight, the ion flight time, was determined by calibration of the ion flight constant, which was determined to be 5.43 μs amu^{-1/2}. In addition, 1.1 microseconds were subtracted from the total time-of-flight to account for the electronic delay between the trigger and the pulse of the photolysis laser. The TOF spectra plotted herein show just the neutral flight time on the horizontal axis; we have subtracted the ion flight time. The time-of-flight spectra are fit using a forward convolution method used to predict the theoretical time-of-flight of the fragments resulting from a given translational energy distribution. The number density distribution of speeds of the molecular beam was determined using a photodepletion or “hole burning” technique. By operating the pulsed valve at 100 Hz and the photolysis laser at 50 Hz, the time-of-flight signal was obtained for the molecular beam with and without the laser. Subtraction of the “laser on” time-of-flight spectrum from the “laser off” time-of-flight spectrum resulted in the time-of-flight spectrum of the molecular beam interacting with the photolysis laser from which the beam speed was determined.

3. Theoretical Calculations of Precursor Geometries and Relative Energies. We use the Gaussian 09 Program, version A.02,⁵³ to perform geometry optimizations, energy calculations, and intrinsic reaction coordinate (IRC) calculations for a variety of species involved in the experiment. Optimized molecular geometries and vibrational frequencies were found using the B3LYP density functional and the 6-311++G(3df,2p) basis. The geometries converged to a root-mean-square (rms) force below 1 × 10⁻⁵ and an rms displacement below 4 × 10⁻⁵, where both are in atomic units. The computation of the zero-point vibrational energies used the B3LYP/6-311++G(3df,2p) vibrational frequencies scaled by 0.9854⁵⁴ as the G4 method required.⁵⁵ For each photolytic

precursor, 1-bromo-2-propanol and 2-bromo-1-propanol, we computationally characterize the equilibrium geometry of each possible conformer and their relative energies. We use these geometries to model the angular momentum imparted to the recoiling radical intermediate. Using the relative energies of the conformers, we determine their relative population in the molecular beam at the temperature of the nozzle. Depending on the type of calculation, the G4 energies have been reported to have a rms deviation between 1.10 to 1.53 kcal/mol when compared to the G3/05 test set.⁵⁵

RESULTS AND ANALYSIS

1. C–Br Bond Fission to Create Nascent C₃H₆OH Radicals. In our study of the OH addition to propene, we begin by creating the two adducts formed from both terminal and central carbon addition in a collision-free environment. To form these adducts with a vibrational energy distribution spanning the barriers to dissociation, we photodissociate a mixture of 1-bromo-2-propanol and 2-bromo-1-propanol with 193 nm photons. We use a velocity map imaging apparatus to characterize the speed and angular distributions of the fragments resulting from photodissociation of the halogenated precursor. Here, we report the measured speed and angular distributions of the recoiling bromine atoms as well as the resulting distribution of kinetic energies imparted to the fragments upon dissociation.

The recoiling bromine atoms originating from the photolytic precursor may be formed in either of two spin–orbit states, ²P_{3/2} or ²P_{1/2}. Using resonance enhanced multiphoton ionization (REMPI), we selectively ionize and detect the recoiling bromine atoms in their respective spin–orbit states. This translational energy distribution is then used to determine the internal energy distribution of the nascent C₃H₆OH radicals.

Figures 1a and 1b show the 2-dimensional ion images of Br(²P_{3/2}) and Br(²P_{1/2}) with the photodissociation laser polarized along the vertical axis; these images are background subtracted and show the signal resulting from 193 nm photodissociation and REMPI ionization. Each image is used to reconstruct the three-dimensional scattering distribution using an inverse Abel transformation in the BASEX Program.⁵⁶ Integrating the three-dimensional velocity distribution over all solid angles at each speed gives the speed distributions, *P*(*v*), for each Br spin–orbit state. The resulting speed distributions (red) and corresponding speed dependence of the anisotropy parameter, β(*v*) (blue), for each spin–orbit state are shown in Figure 1c. The speed dependence of the anisotropy parameter, β(*v*), of the Br(²P_{3/2}) and the Br(²P_{1/2}) atom photoproducts were determined by fitting the measured angular distributions at each speed to $I(\theta) = 1 + \beta_2 P_2(\cos \theta) + \beta_4 P_4(\cos \theta)$, where *P_n* is the *n*th order Legendre polynomial and θ is the angle between the recoil vector and the electric vector of the photolysis laser. The β₄ is relatively small (further details are given in the Supporting Information) for each spin–orbit state, and we therefore approximate the angular distribution to be $I(\theta) = 1 + \beta P_2(\cos \theta)$, where the anisotropy parameter, β, ranges from -1 to 2 with β = -1 corresponding to a perpendicular transition and β = 2 corresponding to a parallel transition. For both Br(²P_{3/2}) and Br(²P_{1/2}), a strong speed dependence is observed with the slower bromine atoms exhibiting β < 0 and faster bromine atoms exhibiting β > 0. However, the rate of the change in β from a more perpendicular transition to a more parallel transition is quite different for each spin orbit state.

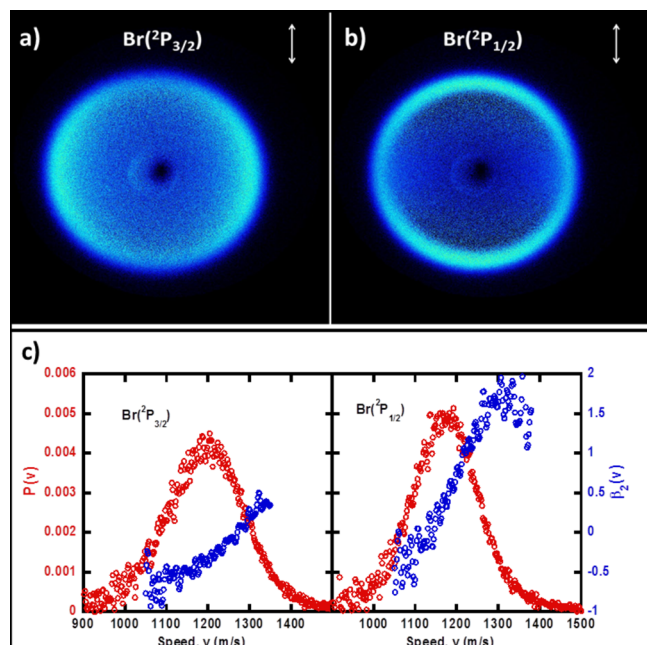


Figure 1. Background-subtracted images for (a) $\text{Br}(^2\text{P}_{3/2})$ and (b) $\text{Br}(^2\text{P}_{1/2})$. The dimensions of the images shown are 928 pixels \times 1040 pixels. The direction of photodissociation laser polarization is shown in the upper right of each image. The lower frame (c) shows the corresponding speed distributions (red) and speed dependence (blue) of the anisotropy parameter $\beta_2(v)$.

Table 1. Anisotropy Parameters

spin-orbit state	anisotropy parameter ^a	$\langle\beta\rangle_{\text{tot}} = f_{\text{Br}^*}(\beta)_{\text{Br}^*} + f_{\text{Br}^{**}}(\beta)_{\text{Br}^{**}}$ ^b
$\text{Br}(^2\text{P}_{3/2})$	$\langle\beta\rangle_{\text{Br}^*} = -0.23$	$\langle\beta\rangle_{\text{tot}} = -0.07$
$\text{Br}(^2\text{P}_{1/2})$	$\langle\beta\rangle_{\text{Br}^{**}} = 0.49$	

^aThe second column gives the average anisotropy parameter, $\langle\beta\rangle$, for each spin-orbit state, determined by averaging over the respective speed distribution. The limits used to integrate over the speed distribution are 1050 to 1380 m/s for $\text{Br}(^2\text{P}_{3/2})$ and 1050 to 1350 m/s for $\text{Br}(^2\text{P}_{1/2})$. The β dependences become too noisy beyond those limits. ^bWeighting the results by the relative fractions of $\text{Br}(^2\text{P}_{3/2})$ and $\text{Br}(^2\text{P}_{1/2})$ (0.77:0.23) yields the total average anisotropy ($\langle\beta\rangle_{\text{tot}}$, third column) for all dissociation events.

Table 1 shows the results of averaging β over the entire speed distribution for each spin-orbit state; the $\text{Br}(^2\text{P}_{3/2})$ atoms result from an excited state with a transition moment perpendicular to the C–Br bond while the $\text{Br}(^2\text{P}_{1/2})$ atoms result from an excited state with a transition moment parallel to the C–Br bond. The results are quite similar to that from the dissociation of 2-bromoethanol⁴² and 2-bromoethanol-*d*₄.⁵⁷ This is also in agreement with the proposed⁵⁸ transitions to the $^1\text{Q}_1$ and the $^3\text{Q}_1$ states resulting in $\text{Br}(^2\text{P}_{3/2})$ and transitions to the $^3\text{Q}_0$ state resulting in $\text{Br}(^2\text{P}_{1/2})$. Weighting the results by the relative fractions of $\text{Br}(^2\text{P}_{3/2})$ and $\text{Br}(^2\text{P}_{1/2})$, the resulting final average β , $\langle\beta\rangle_{\text{tot}}$, for all dissociation events is -0.07 , suggesting that the resulting angular distribution for the $\text{C}_3\text{H}_6\text{OH}$ radicals is quite isotropic.

Figure 2 shows the center of mass recoil translational energy distributions, $P(E_T)$, for $\text{Br}(^2\text{P}_{3/2}) + \text{C}_3\text{H}_6\text{OH}$ and $\text{Br}(^2\text{P}_{1/2}) + \text{C}_3\text{H}_6\text{OH}$, which result from the measured Br velocity distributions using momentum conservation and applying a Jacobian correction. The sum of these kinetic energy distributions, weighted by their spin-orbit branching ratio, gives the total

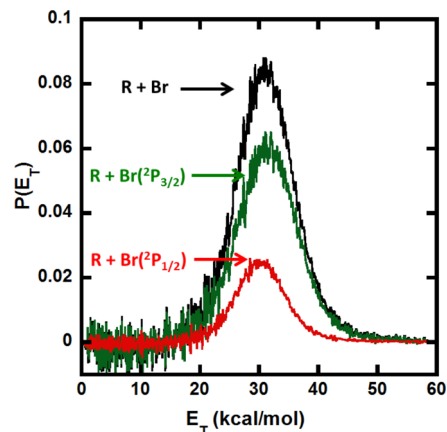


Figure 2. The total relative translational energy distribution for all C–Br photofission events. The figure shows the total (black) relative translational energy distribution, which is the sum of the spin-orbit weighted contributions of the $\text{R} + \text{Br}(^2\text{P}_{3/2})$ (green) $P(E_T)$ and the $\text{R} + \text{Br}(^2\text{P}_{1/2})$ (red) $P(E_T)$ derived from the imaging data in Figure 1.

recoil kinetic energy distribution for $\text{Br} +$ all nascent $\text{C}_3\text{H}_6\text{OH}$ radicals. We determine the spin-orbit branching ratio, $N[\text{Br}(^2\text{P}_{1/2})]/N[\text{Br}(^2\text{P}_{3/2})]$, by integrating the total ion signal from each Br spin-orbit state, $S[\text{Br}(^2\text{P}_{1/2})]$ and $S[\text{Br}(^2\text{P}_{3/2})]$, in images accumulated over the entire Doppler profile, as described in the section on Experimental Methods. We weight the measured signal ratio by the REMPI line strength, $k = 0.32 \pm 0.02$,⁴² as shown in eq 1. The average signal ratio of net ion counts per laser shot for $\text{Br}(^2\text{P}_{1/2})$ and $\text{Br}(^2\text{P}_{3/2})$ was 0.94 ± 0.37 (95% confidence interval), giving a spin-orbit branching ratio for $\text{Br}(^2\text{P}_{1/2})$: $\text{Br}(^2\text{P}_{3/2})$ of 0.30 ± 0.04 . The 95% confidence interval resulted from thirty-seven independent trials. Our total translational energy distribution peaks at 31 kcal/mol and has an average translational energy $\langle E_T \rangle$ of 32.4 kcal/mol. The data here distinguish the fraction of dissociation events that result in $\text{Br}(^2\text{P}_{1/2})$ versus $\text{Br}(^2\text{P}_{3/2})$, which allows us to resolve the internal energy distribution of nascent $\text{C}_3\text{H}_6\text{OH}$ radicals from our measured recoil translational energy distribution.

To confirm the total $P(E_T)$ for C–Br fission derived from the imaging data, we detected a signal at $m/z = 79$ in the scattering apparatus at the NSRRC in Taiwan. Figure 3 shows that data, with the dominant peak near 50 microseconds fit with the $P(E_T)$ shown in black in Figure 2 derived from our imaging data. There is excellent agreement between the two sets of data. Due to its excellent signal-to-noise ratio, the spectrum taken at the NSRRC also revealed a small amount of signal near 100 μs that we tentatively assign to a minor C–Br bond fission mechanism. The $P(E_T)$ shown in Figure 4 that fits this minor channel is derived from forward convolution fitting of the signal shown in the inset of Figure 3. This channel was not apparent in the imaging data because Br atoms formed with these slow speeds ($E_T = 2$ kcal/mol corresponds to $v_{\text{Br}} = 300$ m/s) would have appeared near the center of our imaging detector, where a burn spot obscures the signal. (The Supporting Information shows an example image in which the alignment was moved slightly off center, so a remnant of this signal appears.) To fit the relative signal from fast and slow Br atoms in Figure 3, we weighted the $P(E_T)$ shown in red in Figure 2 by a factor of 186 higher than the minor C–Br bond fission $P(E_T)$, shown in Figure 4.

The nascent radicals formed from the C–Br events resulting in very low relative translational energies (0–4 kcal/mol) have

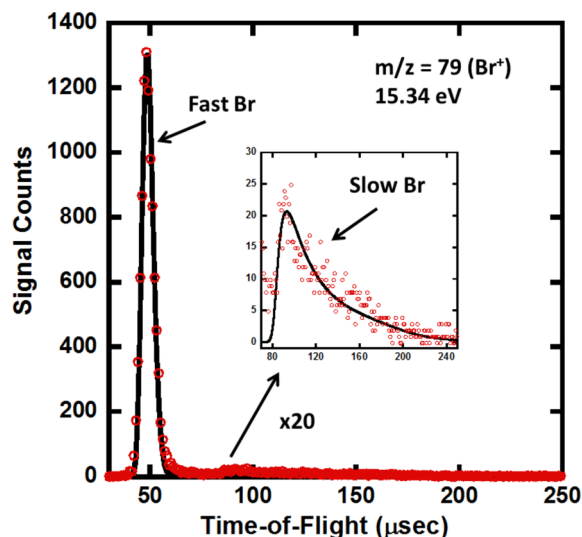


Figure 3. Time-of flight spectrum for $m/z = 79$ fragments. The black fit for the fast peak centered about 50 microseconds is the predicted time-of-flight resulting from the fast C–Br $P(E_T)$ (Figure 2), which was experimentally determined using REMPI detection of the bromine atoms with the velocity map imaging apparatus. The inset shows an expanded view of the TOF spectrum from 70 to 250 microseconds to reveal a tiny contribution from slow Br atoms. The $P(E_T)$ shown in Figure 4 was derived from forward convolution fitting of this region of the TOF. The relative intensities of the fast Br and slow Br contributions was fit by weighting the fast $P(E_T)$ in Figure 2 by a factor of 186 over the $P(E_T)$ for the dissociation events resulting in slow Br atoms shown in Figure 4. The data here was accumulated at a 10° source angle with 15k laser shots. Note the $P(E_T)$ used to fit the portion of the spectrum resulting from fast bromine atoms was not corrected for the preferential detection of photofragments with a more parallel angular distribution, $(1 + \beta/4)$, even though the Br atoms show a speed dependent anisotropy in the velocity map images.

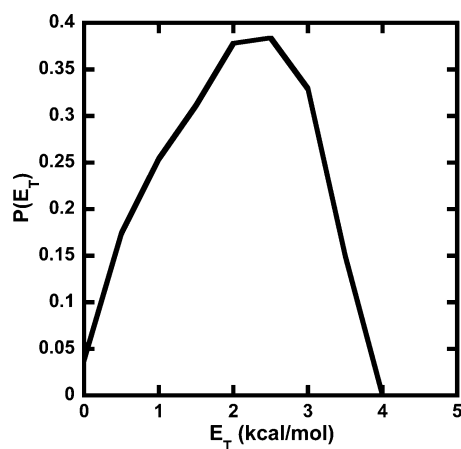


Figure 4. $P(E_T)$ for the slow bromine atoms in the $m/z = 79$ TOF spectrum. This $P(E_T)$ was derived from fitting the minor Br atom signal shown in the inset in Figure 3, assuming the signal resulted from a minor C–Br photofission channel.

very high internal energies and will partition very little of that internal energy to rotational degrees of freedom. Therefore, the nascent C_3H_6OH radicals momentum-matched to the very slow bromine atoms all have vibrational energy above the lowest barrier to dissociation. This, of course, assumes these radicals are created in their ground electronic state, which may not be the case. Electronically excited C_3H_6OH radicals are

such a minor component, however, that products from the dissociation of these radicals are not observed in our spectra. Our spectra are dominated by the unimolecular dissociation products of the radicals produced by the dominant fast C–Br photofission $P(E_T)$ shown in Figure 2.

2. HBr Photoelimination. Figure 5 shows the time-of-flight spectrum for signal with $m/z = 82$ (HBr^+) taken on the

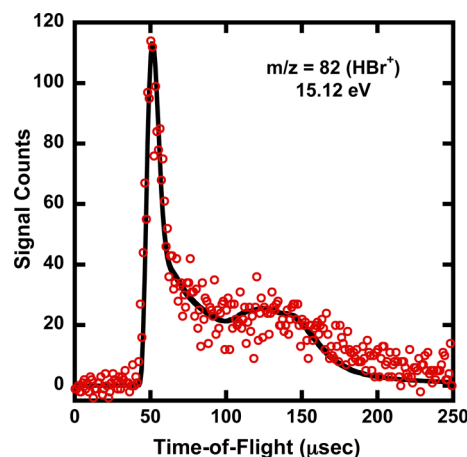


Figure 5. The time-of-flight spectrum for $m/z = 82$ fragments. The fit shown in black results from forward-convolution fitting with the solid black $P(E_T)$ for HBr photoelimination shown in Figure 6. The data here was accumulated at a 10° source angle with 410k laser shots at an ionization energy of 15.12 eV.

scattering apparatus at the NSRRC with a photon ionization energy of 15.12 eV. This signal is assigned to primary HBr photoelimination from both 1-bromo-2-propanol and 2-bromo-1-propanol at 193 nm. The black solid line $P(E_T)$ shown in Figure 6 gives the fit to the data shown in Figure 5. It is clearly

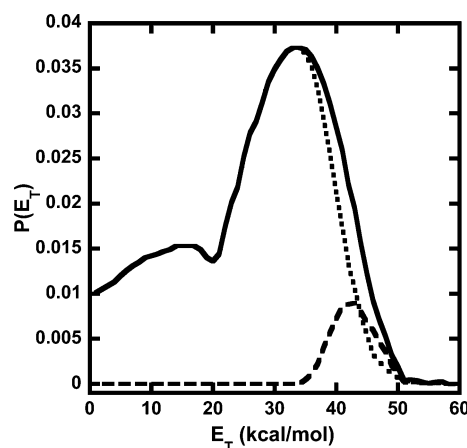


Figure 6. Photofragment recoil kinetic energy distribution (solid black line) for HBr photoelimination. It is used to derive the fit to the $m/z = 82$ TOF spectra in Figure 5. The portion of the $P(E_T)$ shown as the dashed black line was used to derive the fit to the $m/z = 58$ TOF spectra, shown in Figure 9, of the stable mass 58 cofragments to HBr, as the lower kinetic energy cofragments are lost to secondary dissociation. The unstable portion (dotted black line) of the total HBr elimination $P(E_T)$ is derived by subtracting the stable portion from the total.

bimodal, suggesting at least two mechanisms contribute to form HBr photoproducts. There are numerous mechanisms for HBr elimination in each of the two photolytic precursors.

The bromine atom can abstract a hydrogen atom from either the hydroxyl group or from one of the neighboring carbons. The calculated optimized geometries of the potential mass 58 cofragments are given in the Supporting Information along with the HBr elimination endoergicities in Table S1. As the endoergicities of the various HBr eliminations are quite low, many of the resulting cofragments are likely unstable and readily undergo further unimolecular dissociation.

Our data show that some of the unstable cofragments from HBr photoelimination undergo dissociation to methyl and an undetermined fragment with mass 43. We show the $m/z = 43$ TOF spectrum in Figure 7, and we fit this spectrum using the

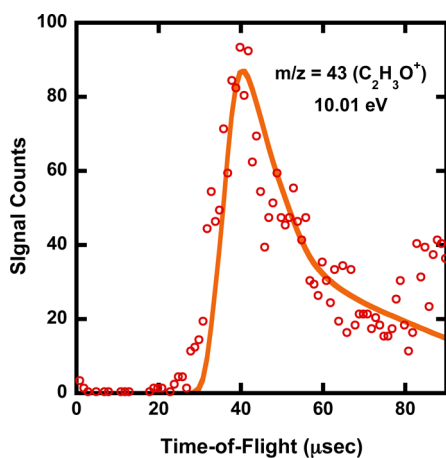


Figure 7. $m/z = 43$ TOF spectra taken at a source angle of 10° with a total of 100k laser shots. The portion of the spectrum shown here from 0–90 μs is the portion of the spectrum containing contributions from the dissociation of unstable mass 58 fragments (those fragments resulting from HBr photoelimination). The full spectrum, which contains a large, slow peak attributed to molecular clusters, is shown in the Supporting Information. The data are shown in red circles. The fit in the orange line is derived from forward convolution fitting using the primary $P(E_T)$ for HBr elimination, shown as the black dotted distribution in Figure 6, and the secondary $P(E_T)$, shown in Figure 8.

black dotted $P(E_T)$ for HBr + $\text{C}_3\text{H}_6\text{O}$ in Figure 6 and the secondary $P(E_T)$ shown in Figure 8 with an isotropic angular distribution. The primary $P(E_T)$ is determined by subtracting the stable mass 58 fragment portion of the $P(E_T)$ from the total, the stable portion (black dashed line in Figure 6) being determined from the $m/z = 58$ TOF spectrum discussed next. The $m/z = 15$ (CH_3^+) TOF spectrum, shown later in this paper, contains contributions from this channel as well as from the dissociation of the 2-hydroxy-1-propyl radicals to acetaldehyde + methyl, discussed in section 5. The portion of the $m/z = 15$ TOF spectrum attributed to the mass 43 + methyl channel is fit using the same set of primary and secondary $P(E_T)$ s used to fit the $m/z = 43$ TOF spectrum. In addition, we show the $m/z = 43$ spectra taken with ionization energies of both 9.2 and 10.01 eV in the Supporting Information, which demonstrate that there is likely no contribution from dissociative ionization of larger fragments.

We also present evidence for the detection of the stable mass 58 cofragments of HBr in the TOF spectrum at $m/z = 58$, shown in Figure 9. This spectrum consists of a fast, sharp peak and a slow, broad peak attributed to clusters (not shown in the figure; the full spectrum is shown in the Supporting Information). The spectrum likely has two contributions: 1) stable mass 58 fragments resulting from HBr photoelimination

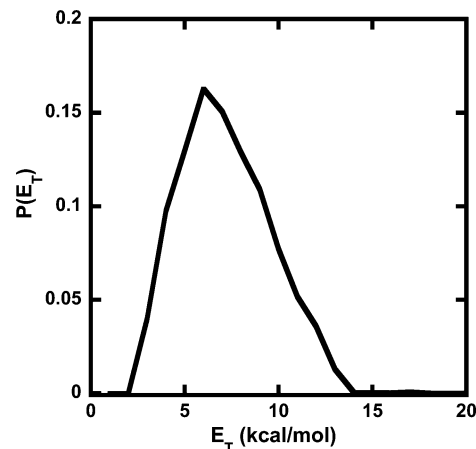


Figure 8. Product recoil kinetic energy distribution resulting from the dissociation of mass 58 fragments (the cofragments to HBr) to $\text{CH}_3 + \text{C}_2\text{H}_3\text{O}$. This secondary $P(E_T)$ is used to generate the orange fit to the $m/z = 43$ TOF spectrum in Figure 7.

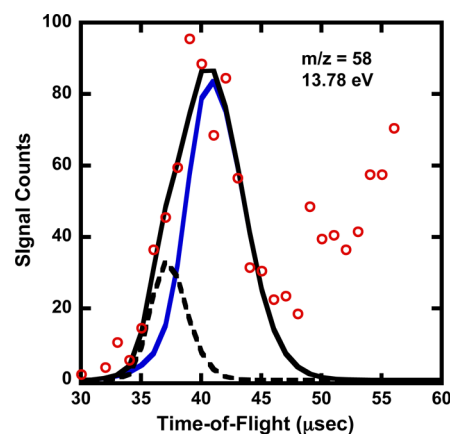


Figure 9. Time-of-flight spectrum taken at $m/z = 58$ ($\text{C}_3\text{H}_5\text{OH}^+$, $\text{C}_3\text{H}_6\text{O}^+$) with a photoionization energy of 13.78 eV. The source angle was 20° , and the signal was accumulated for 800k laser shots. The data are shown in red circles. The contribution shown by the black dashed line is derived from forward-convolution fitting with the $P(E_T)$ for stable mass 58 fragments, which is shown as the black dashed distribution in Figure 6. The blue fit is the contribution resulting from dissociative ionization of the stable $\text{C}_3\text{H}_6\text{OH}$ radicals. The full spectrum, shown in the Supporting Information, also has a large contribution from the dissociation of clusters in the molecular beam.

and 2) dissociative ionization of stable $\text{C}_3\text{H}_6\text{OH}$ radicals resulting from C–Br photofission (calculated appearance energy of 9.97 eV of $\text{CH}_2\text{COHCH}_3^+$ from $\text{CH}_3\text{CH}(\text{OH})\text{CH}_2$; other calculated appearance energies of $m/z = 58$ fragments from $\text{C}_3\text{H}_6\text{OH}$ radicals are given in the Supporting Information). The $P(E_T)$ for the stable $\text{C}_3\text{H}_6\text{OH}$ radicals is discussed in subsection 3, and the blue fit showing the contribution from dissociative ionization of the stable $\text{C}_3\text{H}_6\text{OH}$ radicals still leaves the fast edge of the $m/z = 58$ TOF spectrum quite underfit. By filling this portion in using the black dashed $P(E_T)$ shown in Figure 6 for stable mass 58 fragments, we fit in the remaining portion of the spectrum.

However, the relative weighting of the two contributions is somewhat arbitrary. The fit shown in Figure 9 for the stable mass 58 fragments is an upper bound for the weighting of the mass 58 contribution. To increase the contribution any further would require a broader $P(E_T)$ for stable mass 58 fragments,

which yields a much poorer fit to the $m/z = 43$ spectrum as the fast edge cannot be adequately fit with the resulting unstable mass 58 fragments' $P(E_T)$. We show in the Supporting Information two different fits to the $m/z = 58$ TOF spectrum and the effects of these fits on the fit to the $m/z = 43$ TOF spectrum. One fit assumes the entire $m/z = 58$ spectrum is due only to stable mass 58 fragments. The other fit is similar to that shown in Figure 9, but it has a slightly broader $P(E_T)$ for mass 58 fragments, giving the mass 58 fragments a larger weight. For each case, we determine the unstable mass 58 fragment $P(E_T)$ by subtraction of the stable portion from the total. We show that the majority of the total HBr elimination $P(E_T)$ is required to obtain a good fit to the $m/z = 43$ spectrum because the fast edge cannot be well-fit without fast primary speeds. The effects of the $m/z = 58$ TOF fits on the $m/z = 43$ fits leads us to choose the relative weightings of the two contributions shown in the $m/z = 58$ TOF spectrum in Figure 9.

3. Predictions of Stable Radical $P(E_T)$ s. In our molecular beam experiment, the 1-hydroxy-2-propyl and 2-hydroxy-1-propyl radicals are formed photolytically in a collisionless environment and have a vibrational energy distribution with energies above and below the lowest barrier dissociation channel leading to OH + propene (these barriers are shown in Figures 10 and 11). This photolysis method results in some

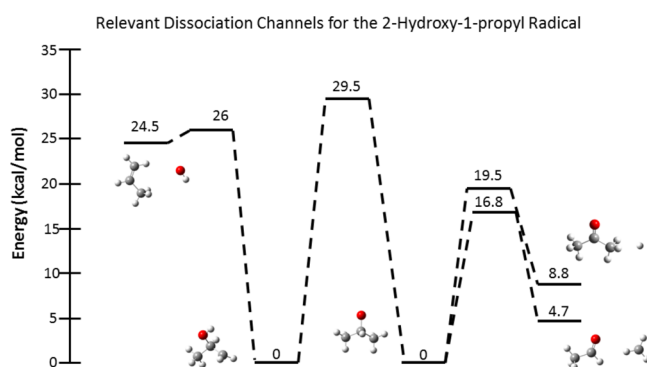


Figure 10. Selected minima and transition states on the potential energy surface for the 2-hydroxy-1-propyl radical. We show the three lowest barrier dissociation channels for the 2-hydroxy-1-propyl radicals: OH + propene with a transition state at 26 kcal/mol, methyl + acetaldehyde with a transition state at 16.8 kcal/mol, and H + acetone with a transition state at 29.5 kcal/mol. The latter two require the 2-hydroxy-1-propyl radical to isomerize over a barrier of 29.5 kcal/mol. The energies are taken from ref 33 and are calculated at the CCSD(T)/cc-pVDZ//B3LYP/cc-pVDZ level of theory.

unstable C_3H_6OH radicals that dissociate to various products as well as C_3H_6OH radicals that are stable to further dissociation. The energy available to the recoiling C_3H_6OH radicals originates from the internal energy of the precursors and the 193 nm photon absorbed by the precursors. Therefore, eq 2 can be used to determine the vibrational energy distribution of the recoiling C_3H_6OH fragments after C–Br fission, provided all other values can be correctly determined.

$$E_{hv} + E_{\text{precursor}} = E_T + D_{0(\text{C-Br})} + E_{\text{vib}} + E_{\text{rot}} + E_{\text{Br}}(^2P_J) \quad (2)$$

E_{hv} represents the energy of the 193 nm photon (148 kcal/mol). $E_{\text{precursor}}$ is the internal energy of the precursor, which we determine by using the thermal distribution of vibrational energies at the nozzle temperature. The precursors' rotational

Relevant Dissociation Channels for the 1-Hydroxy-2-propyl Radical

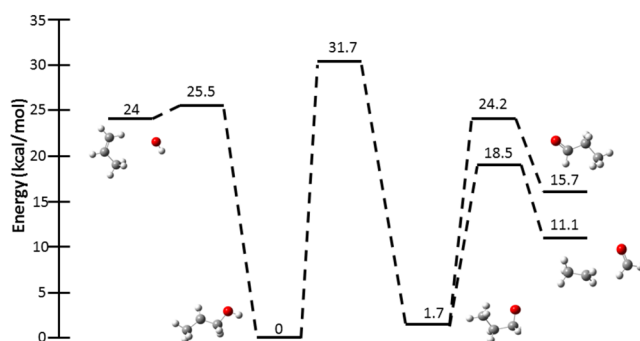


Figure 11. Selected minima and transition states on the potential energy surface for the 1-hydroxy-2-propyl radical. We show the three lowest barrier dissociation channels for the 1-hydroxy-2-propyl radicals: OH + propene with a transition state at 25.5 kcal/mol, ethyl + formaldehyde with a transition state at 18.5 kcal/mol, and H + propanal with a transition state at 24.2 kcal/mol. The latter two require the 1-hydroxy-2-propyl radical to isomerize over a barrier of 31.7 kcal/mol. The energies are taken from ref 33 and are calculated at the CCSD(T)/cc-pVDZ//B3LYP/cc-pVDZ level of theory.

energy is assumed to be negligible as the supersonic expansion of the molecular beam from the nozzle serves to rotationally cool the precursor. E_T is the relative translational energy imparted to the Br and C_3H_6OH fragments upon photodissociation, which is determined by measuring the speed distribution of the recoiling bromine atoms. $D_{0(\text{C-Br})}$ is the C–Br bond dissociation energy for each precursor calculated at the G4//B3LYP/6-311++G(3df,2p) level of theory. These values can be found in Tables 2 and 3. E_{vib} and E_{rot} are the

Table 2. 1-Bromo-2-propanol

conformer	relative energy (kcal/mol) ^a	$D_{0(\text{C-Br})}$ (kcal/mol)	percentage in molecular beam
1(TG)T	0.00	70.07	3.72
1(TG)G	0.15	69.92	2.99
1(TG)G'	-0.05	70.12	3.98
1(G'T)T	0.80	69.27	1.20
1(G'T)G'	-1.69	71.76	41.38
1(G'T)G	1.29	68.78	0.59
1(GG'T)	0.89	69.17	1.04
1(GG'G)	-0.94	71.01	14.23
1(GG'G')	1.29	69.06	0.88

^aThe relative energy of each conformer is with respect to the 1(TG)T conformer.

vibrational and rotational energy, respectively, of the recoiling C_3H_6OH fragments, and $E_{\text{Br}}(^2P_J)$ represents the spin–orbit energy of the recoiling bromine atoms, whose spin–orbit states differ by 10.54 kcal/mol.

For a dissociation of a precursor with a large impact parameter (the perpendicular distance from the impulse vector to the center of mass of the radical) and a relatively heavy atom recoiling away from its cofragment, it is possible that a large fraction of the internal energy is partitioned into the rotation of that cofragment. Consequently, there is less energy available to the vibrational modes of the molecule, resulting in a higher fraction of stable radicals than in the absence of any rotation. To predict the rotational energy imparted to the nascent recoiling C_3H_6OH radicals we use a method similar to that used by Ratliff et al.⁴² and Womack et al.,⁴³ but while their model

Table 3. 2-Bromo-1-propanol

conformer	relative energy (kcal/mol) ^a	D ₀ (C–Br) (kcal/mol)	percentage in molecular beam
2(GG')G'	−0.17	71.34	8.45
2(GG')G	2.52	68.65	0.18
2(TG)G	0.84	70.32	1.97
2(TG)G'	0.99	70.18	1.61
2(TG)T	0.73	70.44	2.32
2(G'T)G'	2.16	69.01	0.30
2(G'T)T	1.73	69.43	0.56
2(G'T)G	−0.56	71.72	14.60

^aThe relative energy of each conformer is with respect to the 1(TG)T conformer.

used the scalar value of inertia, our model includes the full tensor of inertia, as the former is correct only for rotation about a principle axis.⁴⁴ This method uses conservation of angular momentum to determine the amount of rotational energy imparted to the recoiling C₃H₆OH fragments as a function of the recoil velocity vector along the C–Br bond. Neglecting the angular momentum of the photon, electronic angular momentum of the fragments, and rotation of the precursor (all of which are assumed to be negligible), we determine the angular momentum of the recoiling radical intermediate to be given by

$$\vec{J} = \vec{r} \times \vec{p}_{\text{rel}} = \vec{r} \times \mu \vec{v}_{\text{rel}} \quad (3)$$

where \vec{r} is the position vector between the center of mass of the radical moiety in the precursor (using the Franck–Condon geometry in the repulsive excited state) and the bromine atom, and \vec{p}_{rel} is the linear momentum vector taken as a vector along the C–Br bond due to the impulsive force imparted by the photofission. We determine the magnitude of this momentum vector by multiplying the experimental relative velocity by the reduced mass, μ .

For each of our experimentally determined relative velocities, we determine the range of angular momenta imparted to the radical by considering the normal modes of vibration that significantly affect the geometry of the parent molecule, and therefore the impact parameter. Using the harmonic oscillator wave function, we determine the probability of the precursor having various impact parameters. Using eq 3, we develop the angular momentum distribution of the recoiling C₃H₆OH fragments.

We then determine the rotational energy imparted to the C₃H₆OH radicals, which is given by

$$E_{\text{rot}} = \frac{1}{2} \vec{J}^T \Gamma^{-1} \vec{J}, \quad (4)$$

where \vec{J}^T is the transpose of the angular momentum vector and Γ^{-1} is the inverse of the tensor of inertia. Equation 2 may then be used to determine the vibrational energy of the recoiling radical intermediate. We determine the portion of the total C–Br relative translational energy distribution that results in stable C₃H₆OH radicals by selecting those radicals having vibrational energy below the lowest dissociation barrier, shown in Figures 10 and 11, for each E_T . Each photolytic precursor has several conformers which result in C₃H₆OH radicals with different rotational energies (a brief discussion of the conformers is given in Appendix 1, and a more detailed description of the naming scheme is given in Section A in the Supporting

Information). We determine the predicted stable radical $P(E_T)$ s resulting from dissociation of each conformer of the parent molecule (the results for C₃H₆OH radicals from each conformer are shown in the Supporting Information) and weight the results according to the expected thermal population of conformers in the molecular beam (given in Tables 2 and 3). The resulting weighted $P(E_T)$ s are summed together and shown in green in Figure 12.

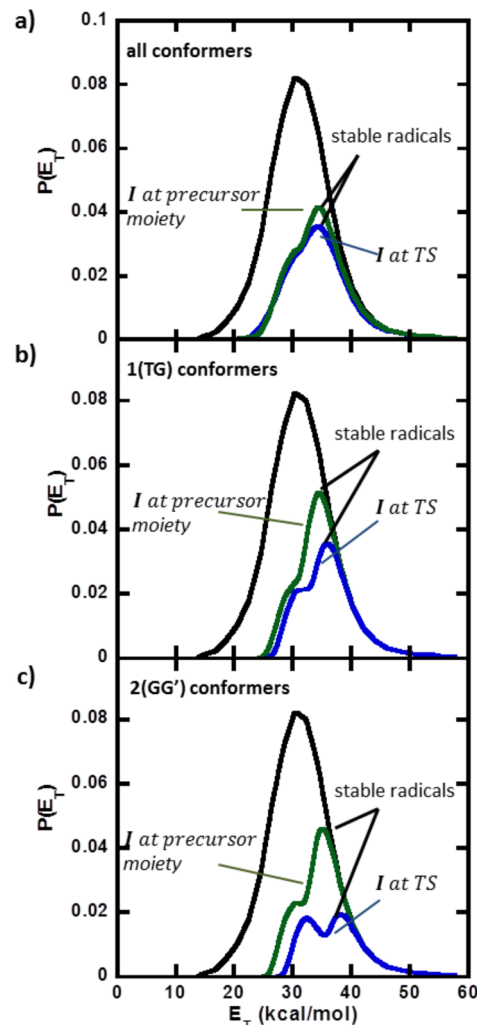


Figure 12. Comparison of the two model predictions for the portion of the C–Br fission $P(E_T)$ that results in stable radicals. The $P(E_T)$ predictions shown in green are the results from using the rotational energy determined from the radical's moiety in the precursor. The $P(E_T)$ predictions shown in blue are the results from determining the rotational energy of the radical at the transition state. The top frame (a) shows the final results from summing the weighted stable C₃H₆OH radical $P(E_T)$ predictions for the dissociation of each group of conformers. The middle (b) and lower (c) frames show the results for the stable C₃H₆OH radical $P(E_T)$ predictions for the dissociation of the 1(TG) and 2(GG') groups of conformers, respectively.

Of course, the geometry of the radical moiety in the photolytic precursor and the equilibrium ground state geometry of the radical are slightly different, and those two geometries will have different tensors of inertia. Likewise, as the radical's geometry changes while approaching a transition state, its tensor of inertia and, hence, its rotational energy changes, which results in a change in vibrational energy. Therefore, we

also predict the stable radical $P(E_T)$ by considering this change in rotational energy as the radical surmounts the transition state barrier.

By mapping the angular momentum vector from its orientation on the radical moiety in the precursor to its orientation on either the transition state geometry or a geometry en route to the transition state, we calculate a centrifugally corrected intrinsic reaction coordinate (IRC) by adding the calculated rotational energy to the $J = 0$ energy at each geometry along the reaction coordinate. We present the corrected IRCs for the C_3H_6OH radicals resulting from the 1(TG) and 2(GG') groups of precursor conformers in Figure 13 for

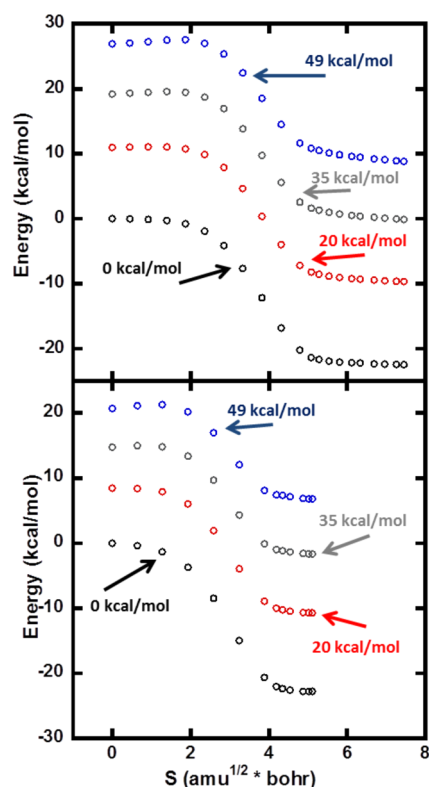


Figure 13. Centrifugally corrected IRCs for the dissociation to OH + propene from the 2-hydroxy-1-propyl (upper frame) and 1-hydroxy-2-propyl (lower frame) radicals resulting from the 1(TG) and 2(GG') groups of conformers, respectively. Each plot shows three corrected IRCs and the $J = 0$ IRC (black) calculated at the B3LYP/6-311++G(3df,2p) level of theory without zero-point correction. The IRCs shown in red are for radicals formed from C–Br fission events that partitioned 20 kcal/mol to E_T . C–Br fission with higher E_T generates radicals with higher rotational energy, so the grey and blue IRCs shown are corrected for $E_T = 35$ and 49 kcal/mol, respectively.

radicals produced from C–Br photofission with three different relative translational energies: 20, 35, and 49 kcal/mol. A complete set of corrected IRCs for the C_3H_6OH radicals resulting from each of the six groups of precursor conformers with translational energies ranging from 20 to 50 kcal/mol is given in the Supporting Information. Because the tensor of inertia changes as the radical geometry approaches the geometry of the transition state, different amounts of rotational energies are added at each point. This phenomenon allows rotationally excited radicals that have vibrational energy just below the $J = 0$ dissociation barrier to possibly surmount the barrier to products because the slight decrease in rotational

energy upon approach to the transition state results in a slight increase in energy available to surmount the barrier. For example, the 1-hydroxy-2-propyl radicals from the 2(GG') precursor show a substantial decrease in rotational energy along the IRC, as shown in Figure 13, lower frame. Additionally, for some of the rotating C_3H_6OH radicals, the location of the maximum along the IRC changes for radicals generated with large relative translational energies. This is the case for the C_3H_6OH radicals resulting from photodissociation of the 1(TG) and 2(GG') conformers of the 1-bromo-2-propanol and 2-bromo-1-propanol conformers, respectively, as shown by Figure 13. Therefore, for those given translational energies, the vibrational energy of the radical at its geometry determined from the corrected IRC maximum is used to determine the stability of the radical rather than at the geometry of the $J = 0$ transition state.

Using this method to determine the rotational energy of the C_3H_6OH radicals which takes into account the change in vibrational and rotational energy during the dissociation process, we again use eq 2 to predict the stable radical $P(E_T)$ for radicals resulting from each conformer, weighting the distributions by the relative conformer population, and summing the results together (the individual results for C_3H_6OH radicals resulting from each conformer is given in the Supporting Information). The final result is given as the blue distribution in Figure 12a. Figures 12b and 12c show comparisons of the $P(E_T)$ predictions for the stable C_3H_6OH radicals resulting from the 1(TG) and 2(GG') groups of conformers, respectively. As expected, the percentage of stable radicals predicted by calculating rotational energy at the radical moiety geometry is slightly larger than the percentage of stable radicals predicted when rotational energy is calculated at a point along the reaction coordinate. We present the predicted percentages of stable radicals resulting from the dissociation of each group of conformers (for both models) in the second column of Table S2 in the Supporting Information. A further in-depth discussion of the determination of the stable radical translational energy distribution using this second method is given in Section B in the Supporting Information.

To test whether our model correctly predicts the portion of the C–Br fission relative translational energy distribution that would result in stable C_3H_6OH radicals, we attempted to detect signal at $m/z = 59$ ($C_3H_6OH^+$) using both the imaging and the scattering apparatus, but no signal was detected. We did, however, detect signal at $m/z = 31$ using each apparatus, which we attribute to the dissociative ionization of the stable radicals. The $m/z = 31$ TOF spectrum, shown in Figure 14, is very well fit by the $P(E_T)$ s in Figure 12. Both model predictions, the one that accounts for the change in rotational energy along the reaction coordinate (blue fit) and the one that does not (green fit), give excellent fits to the measured spectra. Though these two models give visibly different predictions for the radicals from some of the conformers of the photolytic precursors (such as the radicals from the 2(GG') conformers of 2-bromo-1-propanol), once we average over all the conformers of the photolytic precursors present in our experiment, both models give an adequate fit to the data. Other TOF spectra taken to detect the various other product channels also contain contributions from the dissociative ionization of the stable C_3H_6OH radicals, which are fit quite well with the blue predicted $P(E_T)$ in Figure 12. Those spectra are the $m/z = 44$, $m/z = 30$, and $m/z = 29$ TOF spectra, presented in the later

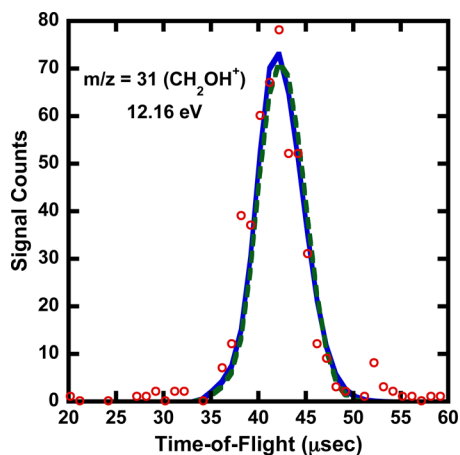


Figure 14. Time-of-flight spectrum detected at $m/z = 31$ taken at a source angle of 20° and accumulated for 50k laser shots. The data are shown as the red circles. The detected fragments are attributed to the dissociative ionization of stable C_3H_6OH radicals (calculated appearance energy of 8.53 eV). Further details of this assignment are presented in the text. The fit in the dashed green line results from the green $P(E_T)$ in Figure 12a. The fit in the solid blue line results from the blue $P(E_T)$ in Figure 12a.

sections covering the dissociation channels of the unstable C_3H_6OH radicals.

We can usually use “soft” photoionization in our imaging apparatus to detect signal at the parent mass, but in the case of stable C_3H_6OH radicals the calculated appearance energy (AE) of $m/z = 31$ is only 8.53 eV. Thus, in our velocity map imaging apparatus we also detected the stable radicals at $m/z = 31$. The image and corresponding speed distribution are given in Figures 15 and 16. In the imaging apparatus, the velocities of

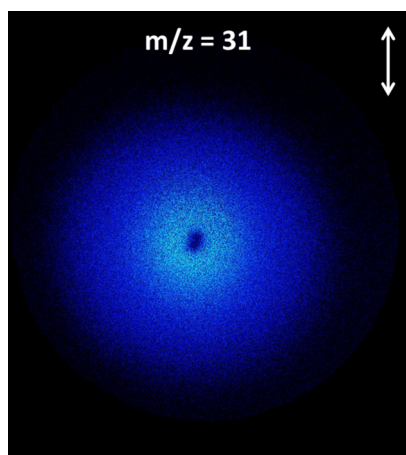


Figure 15. Background-subtracted image for $m/z = 31$ (CH_2OH^+) fragments resulting from dissociative ionization of the stable C_3H_6OH radicals. The dimensions of the image is 928 pixels \times 1040 pixels. The direction of photodissociation laser polarization is shown in the upper right of each image.

the $m/z = 31$ daughter ions are affected by the dissociative ionization, whereas in the scattering apparatus the TOF spectrum reflects only the velocity distribution of the neutral mass 59 fragments (the TOF signals would only differ by the ion flight time, which is subtracted from the spectrum in Figure 14). The ion images result from the vector sum of the velocity imparted to the neutral mass 59 products from C–Br

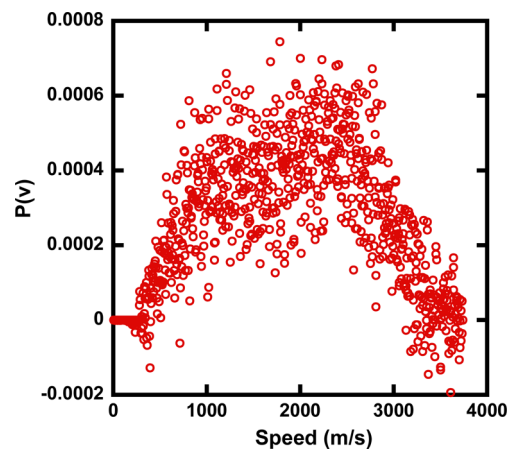


Figure 16. Speed distribution for $m/z = 31$ (CH_2OH^+) fragments derived from the image in Figure 15. The speeds shown here are the net speeds of the $m/z = 31$ fragments, which result from the vector sum of the primary speeds of the stable C_3H_6OH radicals and the secondary speeds imparted to the CH_2OH^+ fragment when the stable C_3H_6OH radicals undergo dissociative ionization to ethene + CH_2OH^+ . The forward–backward scattered nature of the speed distribution presents evidence that the detected ions resulted from the dissociative ionization of rotationally excited radicals.

fission and the additional velocity imparted to the CH_2OH^+ ions upon dissociative ionization of the stable neutral C_3H_6OH radicals. The stable neutral C_3H_6OH radicals are rotationally excited, so the $m/z = 31$ speed distribution in Figure 16 shows the expected bimodality from the forward–backward scattering of the CH_2OH^+ ions as the rotationally excited C_3H_6OH radicals undergo dissociative ionization. The difference between the imaging and scattering speed distributions definitively show that these signals are not from neutral mass 31 products, such as an unlikely dissociation of C_3H_6OH radicals to ethene + CH_2OH ; instead, the signal results from dissociative ionization of the stable C_3H_6OH radicals.

Now that the data have verified the accuracy of predicting which portion of the total C–Br photofission $P(E_T)$ produces stable radicals, we can obtain the portion of the total C–Br relative translational energy distribution resulting in unstable C_3H_6OH radicals by subtracting the stable portion from the total, assuming rotational energy is calculated at the transition state. The resulting stable and unstable portions of the total $P(E_T)$ are given in Figure 17. (The total $P(E_T)$ shown is the same as that shown in Figure 2, but smoothed.) The unstable portion is used to fit the spectra with contributions resulting from the unimolecular dissociation of the unstable radical intermediates to OH + propene.

It is important to emphasize the assumptions made and requirements for the above model. The success of this model relies on the fact that the excited state accessed at 193 nm is repulsive in the C–Br bond in the Franck–Condon region. For certain geometries and high translational energies, this model predicts very high rotational energies, and because of conservation of energy, negative vibrational energies. This is the case for the $1(GG')G$, $1(GG')G'$, and $1(GG')T$ conformers in the high E_T region of the spectrum. We assume that these conformers undergo a change in geometry, likely a slight rotation toward a different conformer, on the excited surface when an impulsive dissociation from the Franck–Condon region would partition too much energy in rotation. This does not alter the prediction of which radicals are formed stable to

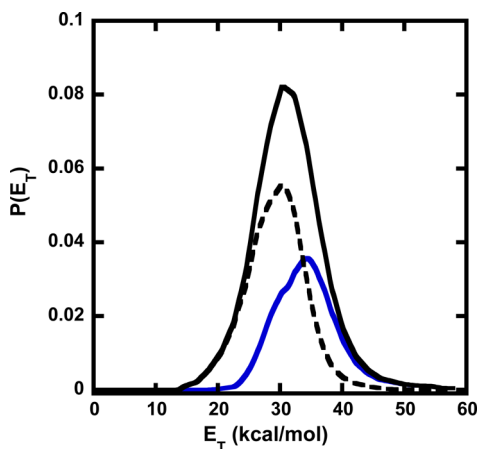


Figure 17. Total C–Br photofission $P(E_T)$ (solid black line) and the portion resulting in stable C_3H_6OH radicals (blue line) and unstable C_3H_6OH radicals (dashed black line). The total C–Br $P(E_T)$ is identical to that in Figure 2, but smoothed. The $P(E_T)$ for stable radicals is the same as the blue distribution in Figure 12a. By taking the difference between the total and stable $P(E_T)$'s, the unstable portion is derived and shown as the dashed black distribution.

subsequent dissociation in our model because the dynamics still result in low vibrational energy radicals, albeit with not quite so much energy in rotation.

4. Dissociation of C_3H_6OH Radicals to OH + Propene.

Figures 10 and 11 show that the lowest calculated dissociation barrier for the 2-hydroxy-1-propyl and 1-hydroxy-2-propyl radicals leads to OH + propene. We characterize this channel by detecting the $m/z = 17$ (OH^+) TOF spectrum and the $m/z = 42$ ($C_3H_6^+$) TOF spectrum, shown in Figure 18. In the fits to these spectra in Figure 18, we assume similar dynamics for all the C_3H_6OH radicals (Next, we present refined fits that allow the radicals with higher rotational energy to partition more energy to translation when they dissociate.) We use the set of primary velocity vectors derived from the unstable portion of the C–Br $P(E_T)$, shown in Figure 17, and the set of secondary velocity vectors derived from the secondary $P(E_T)$ for OH + propene, shown in Figure 19. As each TOF spectrum shows strong forward–backward scattering, we use the distribution of angles between the primary and secondary velocity vectors shown in Figure S35 in the Supporting Information.

We also detected signal at $m/z = 42$ in the imaging apparatus. The image and corresponding net speed distribution are shown in Figures 20 and 21. Using the same primary and secondary $P(E_T)$'s which were used to fit the $m/z = 42$ and $m/z = 17$ TOF spectra, we fit the $m/z = 42$ speed distribution using the forward-convolution procedure described in detail by Allgood et al.;⁵⁹ the corresponding fit is shown in Figure 21.

Because each photolytic precursor has many different conformers resulting in radicals with different rotational excitation, the assumption that all C_3H_6OH radicals have similar dynamics is not entirely valid. The convolution method used here determines the net speeds of the dissociating fragments by assuming the dissociation the C_3H_6OH radicals from each precursor conformer results in the same range of relative speeds between the OH and propene fragments. More realistically, the relative speeds of the propene and OH fragments depend mostly on the tangential velocities of the rotating C_3H_6OH radicals. The unstable radicals with high rotational energy will impart higher relative kinetic energies between the OH and propene fragments (particularly if the axis of rotation is

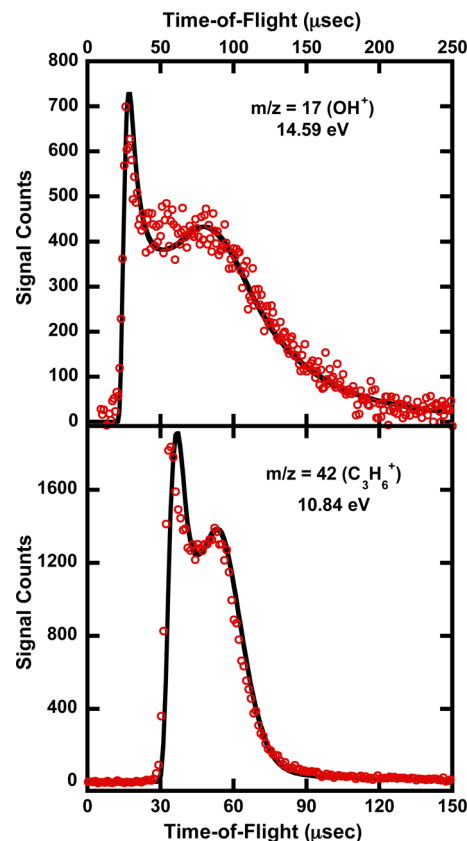


Figure 18. Time-of-flight spectra for the signal at $m/z = 17$, (OH^+) (top frame) accumulated for 200k laser shots, and $m/z = 42$ ($C_3H_6^+$) (lower frame) accumulated with 640k laser shots, both taken at a source angle of 20° . The data are shown as red circles and the fits are shown in black. The fits show these are the momentum-matched OH + propene products from the dissociation of C_3H_6OH radicals, calculating the velocities of the dissociating C_3H_6OH radicals from the unstable portion of the total C–Br $P(E_T)$ (the dashed black distribution in Figure 17), the secondary $P(E_T)$ shown in Figure 19 to calculate the additional velocity imparted to the OH and propene products, and the angular distribution between the two velocity vectors shown in Figure S35 in the Supporting Information.

perpendicular to the vector between the center of mass of the OH and of the propene as they separate) and the unstable radicals with low rotational energy will impart lower relative kinetic energies OH and propene fragments.

In Figure 22, we present the results of our recently developed model⁶⁰ which predicts the net speeds of the OH and propene fragments that result from the dissociation of each conformer, given only the total C–Br $P(E_T)$. This model will be discussed in detail in a future paper, but a brief explanation will be given here. Using the angular momentum vector imparted to a C_3H_6OH radical resulting from the photodissociation of a certain conformer of 1-bromo-2-propanol or 2-bromo-1-propanol, we determine the distribution of tangential velocities of the OH and propene fragments upon dissociation of the C_3H_6OH radical. Each angular momentum vector results in a small range of tangential velocities due to the precession of the angular velocity vector. Thus, the model predicts both the distribution of speeds imparted to the OH and propene fragments when the radical dissociates and the distribution of angles between the C_3H_6OH radical's velocity vector and the corresponding OH and propene fragments' relative velocity vector. This method allows us to determine the net speeds of

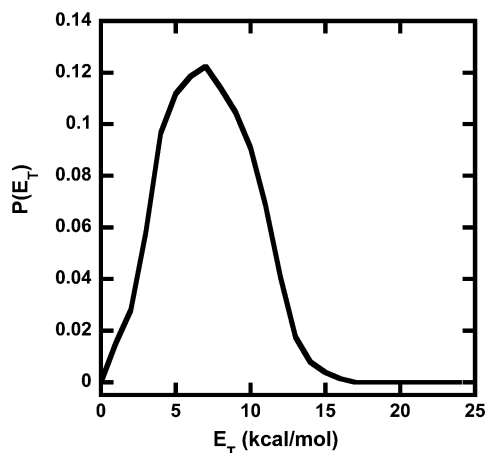


Figure 19. Recoil kinetic energy distribution for the unimolecular dissociation of all unstable C_3H_6OH radicals to $OH +$ propene. In the latter part of this paper, we present a refined treatment of this secondary dissociation that accounts for the larger recoil velocities of the $OH +$ propene from radicals with larger rotational angular momentum.

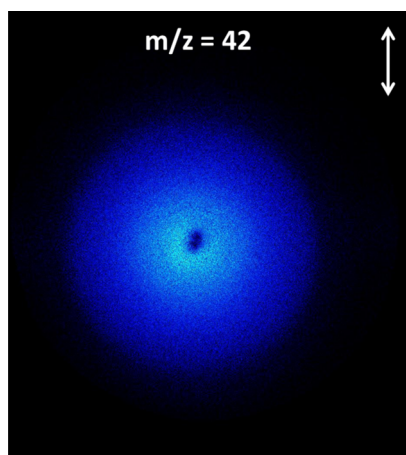


Figure 20. The background-subtracted image for $m/z = 42$ ($C_3H_6^+$) assigned to the propene products resulting from dissociation of the unstable C_3H_6OH radicals. The dimensions of the image is 928 pixels \times 1040 pixels. The direction of photodissociation laser polarization is shown in the upper right of each image.

the OH and propene fragments by performing a small convolution at each primary E_T over just the range of tangential velocities that are correlated to that E_T . Thus, we need not invoke an averaged secondary $P(E_T)$, independent of conformer, to predict the dissociation of the unstable radicals as we did in the fits in Figure 18. Furthermore, and more importantly, the averaged secondary $P(E_T)$ shown in Figure 19 was arbitrarily adjusted for best fit to the data while the new model predicts each secondary $P(E_T)$; these $P(E_T)$ s are not adjusted to achieve a good fit. Nevertheless, the fit shown in Figure 22 is excellent. The improved model shows that the secondary $P(E_T)$ s are very different for each conformer (see Supporting Information), so using an averaged $P(E_T)$ obscures important dynamics. We note that the only variable parameters used to achieve the fit⁶⁰ shown in Figure 22 were the percent contribution from each conformer. The predicted contributions to the OH and propene channel are presented in the third column of Table S2, and the fourth column gives the values

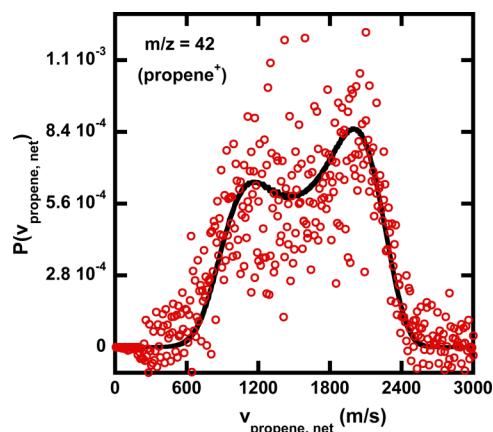


Figure 21. Speed distribution derived from the $m/z = 42$ ($C_3H_6^+$) image. The data are shown by the red circles. The fit shown by the black line results from the vector sum of two velocities, the velocities of the dissociating C_3H_6OH radicals from the unstable radical portion of the $C-Br$ photofission $P(E_T)$ in Figure 17 and the additional velocity imparted to the propene upon dissociation of the radicals calculated from the secondary $P(E_T)$ in Figure 19.

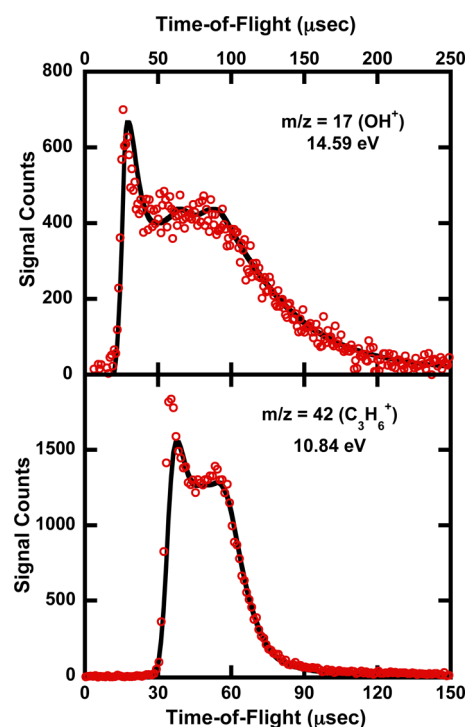


Figure 22. Improved fits of the time-of-flight spectra for the $m/z = 17$ (top) fragments, taken at a source angle of 20° accumulated with 200k laser shots, and $m/z = 42$ (bottom) fragments, taken at a source angle of 20° accumulated with 640k laser shots. The data are shown as red circles. The data is the same as in Figure 18, but the fits results from allowing the tangential velocity of the OH and propene fragments to be correlated to the C_3H_6OH radicals' E_T . We give a brief explanation of the model (ref 60) used to derive these fits in the text, but greater detail will be presented in a future paper.

used to achieve the fit shown in Figure 22. Because this method predicts the net speeds of the propene and OH fragments that result from each conformer, we can test these predictions with experiments on individual conformers. The resulting total net speed distributions for OH and propene are then used to fit the TOF spectra, which are shown in Figure 22.

5. Dissociation of 2-Hydroxy-1-propyl Radicals to Methyl + Acetaldehyde. The calculated transition states in Figure 10 show that, beyond the dissociation barrier to OH + propene, the next lowest barrier for the 2-hydroxy-1-propyl radicals is an isomerization barrier leading to two possible channels: methyl + acetaldehyde and H + acetone. Of these two channels, the barrier to methyl + acetaldehyde is the lowest, and signal at $m/z = 44$ (CH_3CHO^+) and $m/z = 15$ (CH_3^+) was indeed observed. The TOF spectra and fits for these two detected masses are shown in Figure 23. The

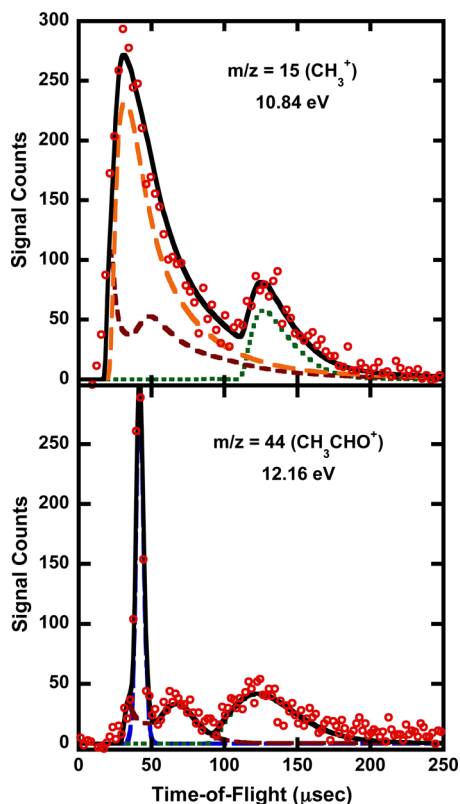


Figure 23. Time-of-flight spectra taken at $m/z = 15$ (top frame) and $m/z = 44$ (lower frame). Each spectrum was taken at a source angle of 10° and accumulated with 300k laser shots. The data are shown as red circles. Each spectrum contains signal from the $\text{CH}_2\text{CH}(\text{OH})\text{CH}_3 \rightarrow \text{CH}_3 + \text{CH}_3\text{CHO}$ channel, shown as the brown dotted line fit in each spectrum. The fits for this channel result from forward convolution of the primary $P(E_T)$ in Figure 24 with the secondary $P(E_T)$ in Figure 25. Each spectrum additionally contains contributions from molecular clusters as shown by the slow peaks in each spectrum, which are fit by the green dotted lines. The $m/z = 15$ spectrum also contains a contribution from the mass 58 $\rightarrow \text{CH}_3 + \text{C}_2\text{H}_5\text{O}$ channel, which is shown by the fit in the dotted orange line. The blue fit, which fits the fast sharp peak in the $m/z = 44$ spectrum is a contribution from dissociative ionization of the stable $\text{C}_3\text{H}_6\text{OH}$ radicals. The total fit for each spectrum is shown by the black solid line.

$m/z = 44$ spectra contains two contributions, one from dissociative ionization of the stable radicals (calculated AE of 10.6 eV) and the second from acetaldehyde resulting from the dissociation of 2-hydroxy-1-propyl radicals. The contribution from dissociative ionization of the stable radicals is clearly observed as a fast sharp peak, and the predicted stable radical $P(E_T)$, shown in Figure 12a as the blue distribution, gives an excellent fit.

By modeling the rotational energy of the nascent 2-hydroxy-1-propyl radicals as described in subsection 3, we determine the

fraction of these radicals having sufficient vibrational energy to surmount the 29.5 kcal/mol isomerization barrier. The predicted $P(E_T)$ for radicals that can surmount this isomerization barrier is given in Figure 24; this is used to derive the set

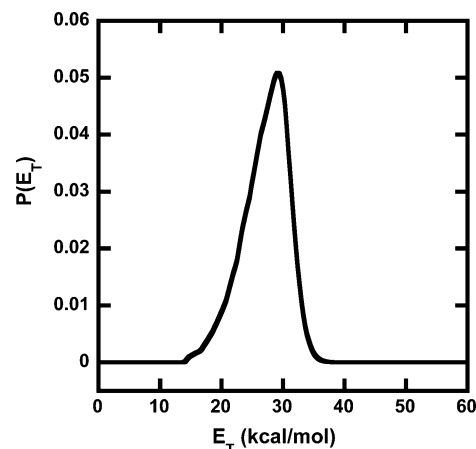


Figure 24. The portion of the C–Br photofission relative translational energy distribution that produces 2-hydroxy-1-propyl radicals with enough vibrational energy to surmount the isomerization barrier en route to the methyl + acetaldehyde channel. This $P(E_T)$ is determined using the method which predicts the rotational energy of the 2-hydroxy-1-propyl radical to be that determined by its moiety in the precursor. As the isomerization involves only a hydrogen shift, the change in moment of inertia is not expected to be significant.

of primary speeds of the 2-hydroxy-1-propyl radicals that dissociate to methyl + acetaldehyde. Of the three main groups of 1-bromo-2-propanol conformers, only the 1(TG) and 1(G'T) groups yield radicals having sufficient energy to dissociate to methyl + acetaldehyde. As these radicals have similar rotational energies, and there is a 12.1 kcal/mol energy difference from the transition state to the methyl + acetaldehyde fragments which likely leads to additional translational energy imparted to the dissociation fragments, we assume one set of primary and secondary $P(E_T)$'s can be used to fit this channel. Using the secondary $P(E_T)$ shown in Figure 25 and the angular distribution given in Figure S36, we fit the portion of the $m/z = 44$ TOF spectrum that cannot be attributed to dissociative ionization of stable radicals.

The signal in the $m/z = 15$ (CH_3^+) TOF spectrum contains contributions from two channels. The first channel was discussed previously in subsection 2. The unstable mass 58 fragments resulting from the primary HBr photoelimination dissociate to mass 43 fragments and methyl. The second contribution is from the methyl + acetaldehyde channel resulting from dissociation of 2-hydroxy-1-propyl radicals. By taking the two sets of $P(E_T)$'s which were determined by the methyl cofragments' TOF spectra ($m/z = 44$ and $m/z = 43$), the total fit for the $m/z = 15$ spectra was determined as the sum of the two contributions. The resulting fit, shown in the top frame of Figure 23, is excellent, confirming the assignment of these product channels.

6. Dissociation of 1-Hydroxy-2-propyl Radicals to Ethyl + Formaldehyde. The calculated transition states in Figure 11 show that, beyond the dissociation barrier to OH + propene, the next lowest barrier for the 1-hydroxy-2-propyl radicals is an isomerization barrier leading to two possible channels: ethyl + formaldehyde and H + propanal. Of these two

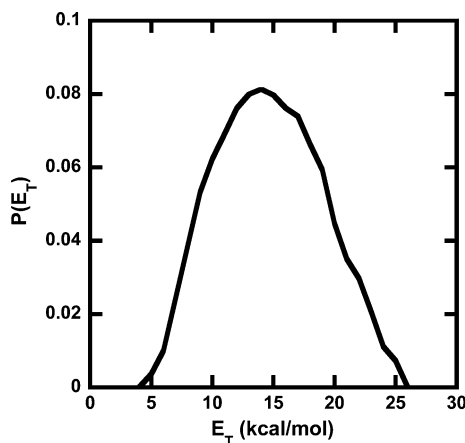


Figure 25. Recoil kinetic energy distribution for the dissociation of 2-hydroxy-1-propyl radicals to methyl + acetaldehyde. This secondary $P(E_T)$ along with the primary $P(E_T)$ in Figure 24 is used to derive the brown fit to the $m/z = 15$ and $m/z = 44$ TOF spectra in Figure 23.

channels, the barrier to ethyl + formaldehyde is the lowest, and signal at $m/z = 29$ ($C_2H_3^+$) and $m/z = 30$ (CH_2O^+) was observed. The TOF spectra and fits for these two detected masses are shown in Figure 26.

To fit the spectra, we first use our model of the rotational energy of the nascent 1-hydroxy-2-propyl radicals to determine the portion of these radicals having sufficient vibrational energy to surmount the 31.7 kcal/mol isomerization barrier. The $P(E_T)$ for these unstable radicals is given in Figure 27, and this is used to derive the set of primary speeds of the 2-hydroxy-1-propyl radicals that dissociate to ethyl + formaldehyde. Of the three main groups of 2-bromo-1-propanol conformers, only the 2(TG) conformers and the 2(G'T) conformers yield radicals having sufficient energy to give notable signal. Of the total ethyl and formaldehyde signal, only 5% is expected to come from the 2(GG') conformers of 2-bromo-1-propanol. Because the radicals resulting from the 2(TG) and the 2(G'T) conformers have similar rotational energies, and there is a 7.4 kcal/mol energy difference from the transition state to the ethyl + formaldehyde fragments (leading to additional translational energy imparted to the dissociation fragments) we assume one set of primary and secondary $P(E_T)$'s can be used to fit this channel. Using the secondary $P(E_T)$ shown in Figure 28 and the angular distribution given in Figure S37, we fit the $m/z = 30$ and $m/z = 29$ spectra. In addition, each spectrum exhibits a sharp peak in the $\sim 40 \mu s$ region, which was assigned to the dissociative ionization of the stable radicals; the calculated AEs are given in eqs 5 and 6.



7. Higher Barrier Dissociation Products. We have thus far considered the lower energy dissociation products of the 1-hydroxy-2-propyl and 2-hydroxy-1-propyl radicals. The remaining higher energy barrier products are all H-loss channels, resulting in various propenol isomers, propanal, and acetone.^{32,33} If significant quantities of these mass 58 fragments were formed, the $m/z = 58$ spectra should have shown some evidence of their presence. Because the H loss would not cause a significant change in the speed of the resulting mass 58 fragments, the unstable portion of the C–Br relative translational energy

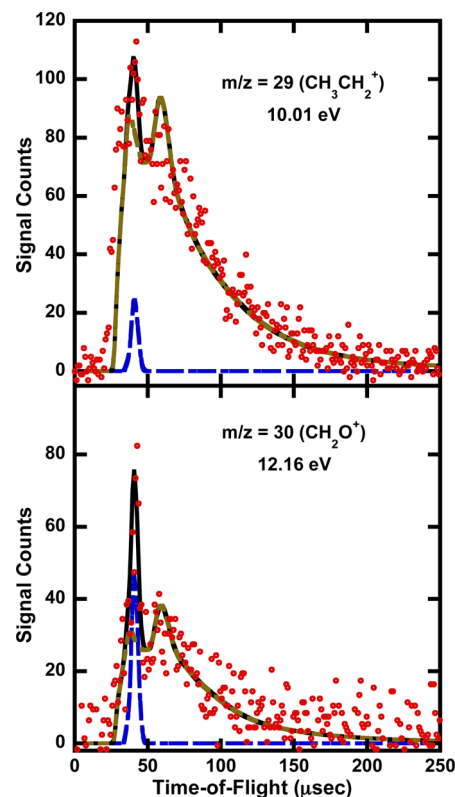


Figure 26. Time-of-flight spectra taken at $m/z = 29$ (top frame) and $m/z = 30$ (lower frame). Each spectrum was taken at a source angle of 20° . The $m/z = 29$ spectrum was accumulated for 450k laser shots and the $m/z = 30$ spectrum was accumulated for 200k laser shots. The data are shown as red circles. Each spectrum contains signal from the $CH_2(OH)CHCH_3 \rightarrow CH_2CH_3 + CH_2O$ channel, shown as the brown dotted line fit in each spectrum. The fits for this channel result from forward convolution of the primary $P(E_T)$ in Figure 27 with the secondary $P(E_T)$ in Figure 28. The blue fit in each spectrum, which fits the fast sharp peak, is a contribution from dissociative ionization of the stable C_3H_6OH radicals. The total fit for each spectrum is shown by the black solid line.

distribution can be used to predict the time-of-flight expected for any propenol, propanol, or acetone fragments. This fit, shown in Figure S40 in the Supporting Information, shows the time-of-flight spectrum predicted assuming signal is from the lowest H-loss barrier channel, H + acetone. The observed $m/z = 58$ signal is much faster than the prediction, so the signal at $m/z = 58$ is likely all due to the stable mass 58 fragments resulting from HBr photoelimination and dissociative ionization of stable C_3H_6OH radicals as mentioned previously in subsection 2. Any portion of the signal which may be due to the propenol, propanal, or acetone fragments is undetectable in our spectrum.

DISCUSSION

The photodissociation of halogenated precursors has long been used to generate radicals for subsequent spectroscopic, kinetics and dynamics experiments. While cooling the nascent radicals produced in this way in a supersonic expansion⁶¹ is advantageous for spectroscopic studies, the studies in our laboratory intentionally create high internal energy radicals in the ground electronic state in order to study their subsequent unimolecular dissociation channels. In this way, we can probe the intermediate steps in bimolecular collisions, such as OH + propene, that proceed through an intermediate well on the global

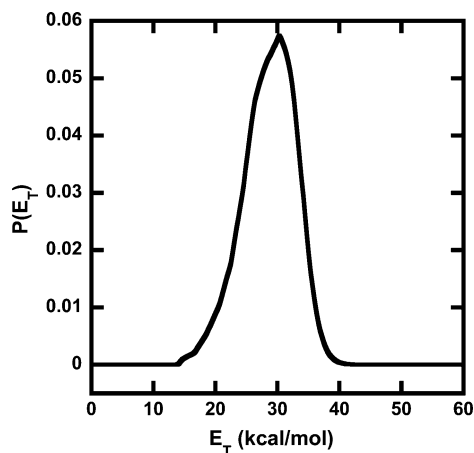


Figure 27. The portion of the C–Br photofission relative translational energy distribution that produces 1-hydroxy-2-propyl radicals with enough vibrational energy to surmount the isomerization barrier en route to the ethyl + formaldehyde channel. This $P(E_T)$ is determined using the method which predicts the rotational energy of the 1-hydroxy-2-propyl radical to be that determined by its moiety in the precursor. As the isomerization involves only a hydrogen shift, the change in moment of inertia is not expected to be significant.

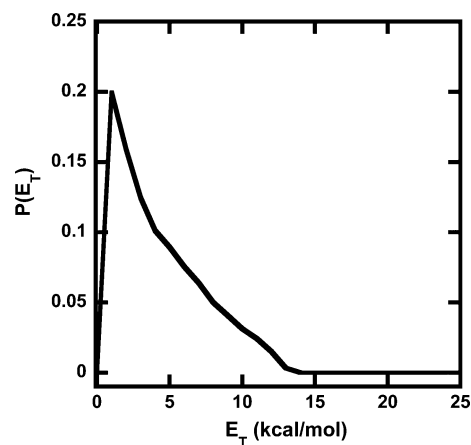


Figure 28. Recoil kinetic energy distribution for the dissociation of 1-hydroxy-2-propyl radicals to ethyl + formaldehyde. This secondary $P(E_T)$ along with the primary $P(E_T)$ in Figure 27 is used to derive the brown fit to the $m/z = 29$ and $m/z = 30$ TOF spectra in Figure 26.

potential energy surface. Thus, our work photodissociates a halogenated precursor not in the expansion region of the nozzle, but rather under collision-free conditions, and then uses velocity measurements of the momentum matched halogen cofragment to determine the internal energy distribution of the resulting radical intermediates.

The OH + propene reaction can proceed through direct H atom abstraction pathways, or via an addition mechanism through highly vibrationally excited radical intermediates en route to the final products of the bimolecular collision. Our work here studied the dissociation of both of these initial radical intermediates, the 2-hydroxy-1-propyl radical that would be formed from OH addition to the end carbon, and the 1-hydroxy-2-propyl radical that would be formed from OH addition to an end C atom. We were able to detect two of the predicted major product channels from these intermediates: $\text{CH}_3 + \text{acetaldehyde}$ from the 2-hydroxy-1-propyl radical and

$\text{C}_2\text{H}_5 + \text{formaldehyde}$ from the 1-hydroxy-2-propyl radical. Both of these product channels result from pathways that begin with isomerization of the hydroxypropyl radical to an isomer where the hydrogen has migrated to a C atom. Our results are in agreement with the transition states for the reaction pathways calculated by Truong and co-workers³³ and by Zador et al.³²

Two key differences between our experiments and a bulk kinetics experiments are that we form the radical intermediates with a well-defined distribution of internal energies and under collision free conditions. Thus, we need not model the inelastic collisions to analyze our results, nor do our products from the radical intermediates include any from bimolecular collisions with other species in the system. This allows us to directly test predictions from theoretical models of these reactions. Of course, this means that the radical intermediates are not stabilized into the intermediate potential energy wells along the reaction coordinates as they would be in a bulk system. In addition, because there are no inelastic collisions to thermalize the rotational degrees of freedom of the radical intermediate, the angular momentum of the radical intermediate is defined by the photodissociation dynamics that created them. We use this fact in this paper to assess the partitioning of the nascent radical's energy between rotation and vibration. Importantly, we have used the current results to test a model for this energy partitioning, paying close attention to the direction of orbital angular momentum in the nascent radicals and how the rotational energy in the radicals changes along the relevant intrinsic reaction coordinates. This is important information for testing theoretical predictions for the unimolecular dissociation channels. While statistical unimolecular reaction rate theories such as RRKM theory often assume the rotational degrees of freedom are thermalized, to compare our experimental results with theoretical predictions we must define the direction and magnitude of the angular momentum vector in our nascent radicals. Our recent quasiclassical trajectory calculations⁴⁴ on the dissociation dynamics of the β -hydroxyethyl radical have treated the angular momentum in the nascent radicals correctly,⁶² but this is often ignored in comparing theory to experiment.

The OH + propene system studied here is rich not only because there are two radical intermediates important in the reaction, but also because the photolytic production of the radical intermediates includes dynamics controlled by the particular conformer of the photolytic precursor involved. Using the impulsive model to predict the rotational energy of the $\text{C}_3\text{H}_6\text{OH}$ fragments, we predicted the $P(E_T)$ of the stable $\text{C}_3\text{H}_6\text{OH}$ radicals by selecting the radicals having vibrational energy below the lowest barrier to dissociation. We presented two different stable radical $P(E_T)$'s, one which assumes the rotational energy stays constant throughout the dissociation process and one which assumes the rotational energy changes throughout the dissociation process. Because the change in geometry along the reaction coordinate results in different tensors of inertia, the rotational energy should change during the dissociation, which would result in a corresponding change in the energy available to surmount the calculated dissociation barriers. The effect is marked for the radicals from select conformers of the photolytic precursors, but the resulting predictions for the stable radical spectrum are similar once the prediction is averaged over all the precursor conformers. Furthermore, since the transition state involved in the dissociation of $\text{C}_3\text{H}_6\text{OH}$ radicals to OH + propene proceeds through a bridged-like van der Waals complex, the moment of inertia of the dissociating molecule does not change as

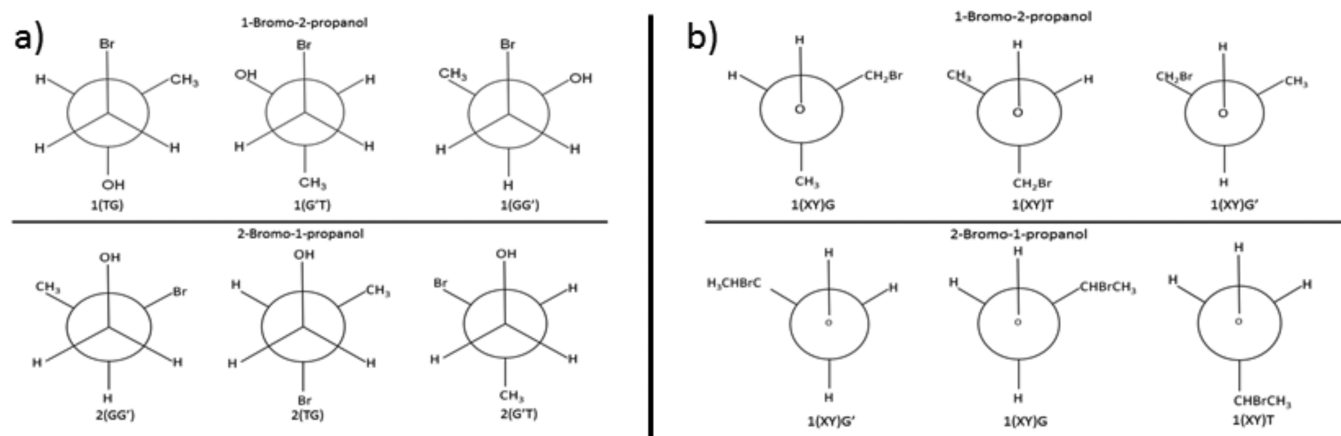


Figure 29. (a) Newman projections for the six sets of conformers of the two photolytic precursors, 1-bromo-2-propanol and 2-bromo-1-propanol. Each Newman projection looks down the terminal carbon/center carbon axis. The labels in parentheses are the *Gauche* and *Trans* relationships between the terminal carbon substituent and the center carbon substituents as defined in the text. (b) Newman projections for the various precursor conformers. They show the dihedral angle between the hydrogen on the hydroxyl group and the carbon which is bonded to the bromine atom. The upper three diagrams show the three possibilities for the 1-bromo-2-propanol precursor, and the lower three diagrams show the three possibilities for the 2-bromo-1-propanol precursor.

significantly as it would for a more typical dissociation proceeding through a simple bond stretch. The results of this model, however, agree very well with the data. The predicted stable radical $P(E_T)$ fits the TOF spectra containing contributions from dissociative ionization of the stable C_3H_6OH radicals quite well. The results certainly provides motivation to continue testing these two models against each other, especially for systems with less rotational complexity and larger changes in the moment of inertia during dissociation. For systems with those criteria, the differences in the two models would be expected to manifest more noticeably.

We also presented data on the dissociation of the unstable C_3H_6OH radical intermediates to three different dissociation channels, $OH +$ propene, acetaldehyde + CH_3 , and ethyl + formaldehyde. The detected products in each channel were momentum-matched. Each spectrum evidence a strongly forward–backward scattered, but symmetric angular distribution, indicating the radical undergoes many rotations prior to dissociation. These angular distributions are similar to those measured for the dissociation products of rotationally excited C_2H_4OH radicals.^{50,63}

Dissociation of the rotationally excited C_3H_6OH radicals to OH and propene offered the opportunity to test our recently developed model, which predicts the tangential velocities and angular distributions of the products. The results of this model demonstrated that the OH and propene speed distributions differ markedly for C_3H_6OH radicals with different angular momenta. While trajectory calculations are capable of yielding results that agree well with experimental data, such as those performed by McKown et al.,⁴⁴ they require a global potential energy surface and a very large number of trajectories to obtain good statistical results. The model used to fit the OH and propene TOF spectra in this study does not need a global potential energy surface, nor a large number of trajectories. The results, however, agree quite well with the data, especially considering there were no adjustable parameters except for the relative contributions to the OH and propene signal resulting from the dissociation of each conformer. These did not deviate substantially from the expected quantities (see Table S2 in the Supporting Information). Note that the calculations require an experimentally determined $C-Br$ $P(E_T)$, and they rely on

exciting the photolytic precursor to a repulsive excited state. They are also only applicable to dissociation channels with no barrier beyond the endoergicity. A more detailed description of this model will be presented in a future paper.⁶⁰

The dissociation of the 2-hydroxy-1-propyl radicals to acetaldehyde + CH_3 and the dissociation of the 1-hydroxy-2-propyl radicals to ethyl + formaldehyde also exhibit effects from the rotational excitation of the C_3H_6OH radicals. The 2-hydroxy-1-propyl radicals result from the photodissociation of 1-bromo-2-propanol molecules, the conformers of which have large impact parameters. Therefore, many of the 2-hydroxy-1-propyl radicals have high rotational energy as a result of the photodissociation. The difference in energy from the dissociation transition state to the acetaldehyde + methyl products is about 12 kcal/mol, so one would expect a rotationally cold 2-hydroxy-1-propyl radical to dissociate to yield methyl + acetaldehyde fragments with a range of relative translational energies not exceeding 12 kcal/mol. The $P(E_T)$ for the dissociation of 2-hydroxy-1-propyl to methyl + acetaldehyde that fits the $m/z = 44$ (acetaldehyde⁺) TOF spectrum, however, ranges from 5–25 kcal/mol, the additional speed resulting from the tangential velocity of the rotating 2-hydroxy-1-propyl radical.

As for the 1-hydroxy-2-propyl radicals, they result from the photodissociation of 2-bromo-1-propanol, whose conformers have small impact parameters, which leads to lower rotational excitation of the radicals. Additionally, only the 1-hydroxy-2-propyl radicals with lower translational energy have enough vibrational energy to surmount the isomerization barrier en route to the ethyl + formaldehyde dissociation products. The expected maximum relative translational energy for ethyl + formaldehyde fragments resulting from the dissociation of rotationally cold 1-hydroxy-2-propyl radicals is not expected to exceed 7 kcal/mol based on the energy difference from the transition state to products. The $P(E_T)$ for the dissociation of 1-hydroxy-2-propyl to ethyl + formaldehyde that fits the $m/z = 29$ (ethyl⁺) and $m/z = 30$ (CH_2O^+) TOF spectra, however, ranges from 0–13 kcal/mol; the modest additional speed may result from the tangential velocity of the rotating 1-hydroxy-2-propyl radicals.

One interesting product channel which we were unable to explore experimentally was a possible branching to an $\text{H}_2\text{O} +$ propenyl channel from the radical intermediate. Our prior work on $\text{OH} +$ ethene detected a substantial branching to the analogous $\text{H}_2\text{O} +$ vinyl channel from the β -hydroxy radical, despite the absence of a direct pathway linking the two.⁴² Quasiclassical trajectory calculations⁴⁴ confirm that a likely route to these products is one where the OH starts to separate from the alkene en route to the $\text{OH} +$ alkene product channel, but interacts in the exit channel with the forming alkene moiety to abstract an H atom. An analogous pathway is possible in the $\text{OH} +$ propene system, but we were unable to find experimental evidence.

In addition, our data showed no evidence of the higher energy H -loss channels, which should have given signal in the $m/z = 58$ TOF spectrum. To successfully probe these channels, we would need to generate $\text{C}_3\text{H}_6\text{OH}$ radicals with a higher range of vibrational energies. Our future experiments on the reaction between OH and propene through a $\text{C}_3\text{H}_6\text{OH}$ addition complex will involve photodissociation of a pure sample of 2-chloro-1-propanol at 157 nm, which will likely produce radicals with less rotational energy and higher vibrational energies. This will allow for the potential detection of the higher barrier channels. A study of the experimentally determined branching ratio of products resulting from the dissociation of the 1-hydroxy-2-propyl radicals will enable us to compare with the theoretical RRKM branching ratios.

■ APPENDIX

A1: Conformers of 1-Bromo-2-propanol and 2-Bromo-1-propanol

Here, we briefly discuss the various conformers of the two photolytic precursors, 1-bromo-2-propanol and 2-bromo-1-propanol. Each 1-bromo-2-propanol and 2-bromo-1-propanol molecule has several conformers, resulting in different angular momenta being imparted to the $\text{C}_3\text{H}_6\text{OH}$ radicals upon photodissociation. Figure 29a shows the Newman projections for each group of conformers along the terminal $\text{C}-\text{C}$ bond. Figure 29b shows the Newman projections along the $\text{O}-\text{C}$ bond for each conformer group. While the position of the hydrogen on the hydroxyl group does not substantially affect the angular momentum imparted to the $\text{C}_3\text{H}_6\text{OH}$ radicals, it does affect the relative stability of one conformer over the other. Tables 2 and 3 list the relative energies, $\text{C}-\text{Br}$ dissociation energies, and the expected populations in the molecular beam for each conformer. A more detailed discussion may be found in Section A of the Supporting Information.

■ ASSOCIATED CONTENT

Supporting Information

Notation scheme for naming the 1-bromo-2-propanol and 2-bromo-1-propanol conformers, detail on the computational method for predicting the portion of the total $\text{C}-\text{Br}$ $P(E_T)$ resulting in stable $\text{C}_3\text{H}_6\text{OH}$ radicals, additional images for Br^+ , β_4 speed dependence, centrifugally corrected IRCs for the dissociation of the $\text{C}_3\text{H}_6\text{OH}$ radical to OH and propene, additional TOF spectra for $m/z = 43$ and $m/z = 58$, calculated geometries for the various 1-bromo-2-propanol and 2-bromo-1-propanol conformers, stable radical $P(E_T)$ predictions resulting from the dissociation of each group of conformers, trial fits of $m/z = 58$ and $m/z = 43$ to determine the stable and unstable portions of the total HBr elimination $P(E_T)$, angular

distributions between the primary and secondary velocity vectors for the dissociation of $\text{C}_3\text{H}_6\text{OH}$ radicals, predicted secondary $P(E_T)$ s and angular distributions for the dissociation of $\text{C}_3\text{H}_6\text{OH}$ radicals to OH and propene resulting from the 1(TG) and 2(GG') groups of conformers, and TOF prediction for the lowest barrier H -loss channel on the $m/z = 58$ TOF spectrum. This material is available free of charge via the Internet at <http://pubs.acs.org>.

■ AUTHOR INFORMATION

Corresponding Author

*(L.J.B.) E-mail: l-butler@uchicago.edu. Telephone: 773-702-7206.

Notes

The authors declare no competing financial interest.

■ ACKNOWLEDGMENTS

This work was supported by the Chemical Sciences, Geosciences and Biosciences Division, Office of Basic Energy Sciences, Office of Science, U.S. Department of Energy, under Grant No. DE-FG02-92ER14305 (L.J.B.). Synchrotron beam time and additional funding were provided by the National Synchrotron Radiation Research Center and Academia Sinica. We gratefully acknowledge the invaluable help at the NSRRC from Dr. Bing Jin.

■ REFERENCES

- (1) Zellner, R.; Lorenz, K. Laser Photolysis/Resonance Fluorescence Study of the Rate Constants for the Reactions of Hydroxyl Radicals with Ethene and Propene. *J. Phys. Chem.* **1984**, *88*, 984–989.
- (2) Klein, T.; Barnes, I.; Becker, K. H.; Fink, E. H.; Zabel, F. J. Pressure Dependence of the Rate Constants for the Reactions of Ethene and Propene with Hydroxyl Radicals at 295 K. *Phys. Chem.* **1984**, *88*, S020–S025.
- (3) Tully, F. P.; Goldsmith, J. E. M. Kinetic Study of the Hydroxyl Radical-Propene Reaction. *Chem. Phys. Lett.* **1985**, *116*, 345–352.
- (4) Atkinson, R.; Pitts, J. N. Rate Constants for the Reaction of OH Radicals with Propylene and the Butenes Over the Temperature Range 297 – 425 °K. *J. Chem. Phys.* **1975**, *63*, 3591–3595.
- (5) Ravishankara, A. R.; Wagner, S.; Fischer, S.; Smith, G.; Schiff, R.; Watson, R. T.; Tesi, G.; Davis, D. D. A Kinetics Study of the Reactions of OH with Several Aromatic and Olefinic Compounds. *Int. J. Chem. Kinet.* **1978**, *10*, 783–804.
- (6) Hoyermann, K.; Sievert, R. Die Reaktion von OH -Radikalen mit Propen: I. Bestimmung der Primärprodukte bei niedrigen Drücken. *Ber. Bunsen-Ges. Phys. Chem.* **1979**, *83*, 933–939.
- (7) Biermann, H. W.; Harris, G. W.; Pitts, J. N. Photoionization Mass Spectrometer Studies of the Collisionally Stabilized Product Distribution in the Reaction of Hydroxyl Radicals with Selected Alkenes at 298 K. *J. Phys. Chem.* **1982**, *86*, 2958–2964.
- (8) Nip, W. S.; Paraskevopoulos, G. Rates of OH Radical Reactions. VI. Reactions with C_3H_6 , $1-\text{C}_4\text{H}_8$ and $1-\text{C}_5\text{H}_{10}$ at 297 K. *J. Chem. Phys.* **1979**, *71*, 2170–2174.
- (9) Lloyd, A. C.; Darnall, K. R.; Winer, A. M.; Pitts, J. N. Relative Rate Constants for Reaction of the Hydroxyl Radical with a Series of Alkanes, Alkenes, and Aromatic Hydrocarbons. *J. Phys. Chem.* **1976**, *80*, 789–794.
- (10) Wu, C. H.; Japar, S. M.; Niki, H. Relative Reactivities of HO -Hydrocarbon Reactions from Smog Reactor Studies. *J. Environ. Sci. Health. A.* **1976**, *11*, 191–200.
- (11) Winer, A. M.; Lloyd, A. C.; Darnall, K. R.; Pitts, J. N. Relative Rate Constants for the Reaction of the Hydroxyl Radical with Selected Ketones, Chloroethanes, and Monoterpene Hydrocarbons. *J. Phys. Chem.* **1976**, *80*, 1635–1639.
- (12) Winer, A. M.; Lloyd, A. C.; Darnall, K. R.; Atkinson, R.; Pitts, J. N. *Chem. Phys. Lett.* **1977**, *51*, 221–226.

- (13) Cox, R. A.; Derwent, R. G.; Williams, M. R. Atmospheric Photooxidation Reactions. Rates, Reactivity, and Mechanism for Reaction of Organic Compounds with Hydroxyl Radicals. *Environ. Sci. Technol.* **1980**, *14*, 57–61.
- (14) Barnes, I.; Bastian, V.; Becker, K. H.; Fink, E. H.; Zabel, F. Studies of Organic Substances towards Hydroxyl Radicals under Atmospheric Conditions. *Atmos. Environ.* **1982**, *16*, 545–550.
- (15) Barnes, I.; Bastian, V.; Becker, K. H.; Fink, E. H.; Nelsen, W. Oxidation of Sulphur Compounds in the Atmosphere: I. Rate Constants of OH Radical Reactions with Sulphur Dioxide, Hydrogen Sulphide, Aliphatic Thiols, and Thiophenol. *J. Atmos. Chem.* **1986**, *4*, 445–466.
- (16) Atkinson, R.; Aschmann, S. M. Rate Constants for the Gas-Phase Reactions of the OH Radical with a Series of Aromatic Hydrocarbons at 296 ± 2 K. *Int. J. Chem. Kinet.* **1989**, *21*, 355–365.
- (17) Schmidt, V.; Zhu, G. Y.; Becker, K. H.; Fink, E. H. Study of OH Reactions at High Pressures by Excimer Laser Photolysis-Dye Laser Fluorescence. *Ber. Bunsen-Ges. Phys. Chem.* **1985**, *89*, 321–322.
- (18) Wallington, T. J. Kinetics of the Gas Phase Reaction of OH Radicals with Pyrrole and Thiophene. *Int. J. Chem. Kinet.* **1986**, *18*, 487–496.
- (19) Nielsen, O. J.; Jorgensen, O.; Donlon, M.; Sidebottom, H. W.; O'Farrell, D. J.; Treacy, J. Rate Constants for the Gas-Phase Reactions of OH Radicals with Nitroethene, 3-Nitropropene and 1-Nitrocyclohexene at 298 K and 1 atm. *Chem. Phys. Lett.* **1990**, *168*, 319–323.
- (20) Liu, A. The Gas-Phase Reaction of Hydroxyl Radicals with Several Unsaturated Hydrocarbons. *J. Radiat. Res. Radiat. Process.* **1990**, *8*, 28–32.
- (21) Morris, E. D.; Stedman, D. H.; Niki, H. Mass-spectrometric Study of the Reactions of the Hydroxyl Radical with Ethylene, Propylene, and Acetaldehyde in a Discharge-flow System. *J. Am. Chem. Soc.* **1971**, *93*, 3570–3572.
- (22) Bradley, J. N.; Hack, W.; Hoyermann, K.; Wagner, H. G. Kinetics of the Reaction of Hydroxyl Radicals with Ethylene and with C_3 Hydrocarbons. *J. Chem. Soc. Faraday Trans. 1* **1973**, *69*, 1889–1898.
- (23) Stuhl, F. Determination of Rate Constants for the Reactions of OH with Propylene and Ethylene by a Pulsed Photolysis-Resonance Fluorescence Method. *Ber. Bunsen-Ges. Phys. Chem.* **1973**, *77*, 674–677.
- (24) Gorse, R. A.; Volman, D. H. Photochemistry of the Gaseous Hydrogen Peroxide-Carbon Monoxide System II: Rate Constants for Hydroxyl Radical Reactions with Hydrocarbons and for Hydrogen Atom Reactions with Hydrogen Peroxide. *J. Photochem.* **1974**, *3*, 115–122.
- (25) Gordon, S.; Mulac, W. A. Reaction of the $OH(X^2\Pi)$ Produced by the Pulse Radiolysis of Water Vapor. *Int. J. Chem. Kinet., Symp.* **1975**, *1*, 289–299.
- (26) Pastrana, A. V.; Carr, R. W. Kinetics of the Reaction of Hydroxyl Radicals with Ethylene, Propylene, 1-Butene, and *trans*-2-Butene. *J. Phys. Chem.* **1975**, *79*, 765–770.
- (27) Smith, R. H. Rate Constant for the Gaseous Reaction between Hydroxyl and Propene. *J. Phys. Chem.* **1983**, *87*, 1596–1600.
- (28) Vasu, S. S.; Hong, Z.; Davidson, D. F.; Hanson, R. K.; Golden, D. M. Shock/Laser Absorption Measurements of the Reaction Rates of OH with Ethylene and Propene. *J. Phys. Chem. A* **2010**, *114*, 11529–11537.
- (29) Bott, J. F.; Cohen, N. A Shock Tube Study of the Reactions of the Hydroxyl Radical with Several Combustion Species. *Int. J. Chem. Kinet.* **1991**, *23*, 1075–1094.
- (30) Vakhtin, A. B.; Lee, S.; Heard, D. E.; Smith, I. W. M.; Leone, S. R. Low-Temperature Kinetics of Reactions of the OH Radical with Propene and 1-Butene Studied by a Pulsed Laval Nozzle Apparatus Combined with Laser-Induced Fluorescence. *J. Phys. Chem. A* **2001**, *105*, 7889–7895.
- (31) Spangenberg, T.; Hohler, S.; Hansmann, B.; Wachsmuth, U.; Abel, B. Low-Temperature Reactions of OH Radicals with Propene and Isoprene in Pulsed Laval Nozzle Expansions. *J. Phys. Chem. A* **2004**, *108*, 7527–7534.
- (32) Zador, J.; Jasper, A. W.; Miller, J. A. The Reaction between Propene and Hydroxyl. *Phys. Chem. Chem. Phys.* **2009**, *11*, 11040–11053.
- (33) Huynh, L. K.; Zhang, H. R.; Zhang, S.; Eddings, E.; Sarofim, A.; Law, M. E.; Westmoreland, P. R.; Truong, T. N. Kinetics of Enol Formation from Reaction of OH with Propene. *J. Phys. Chem. A* **2009**, *113*, 3177–3185.
- (34) Zhou, C.; Li, Z.; Li, X. Kinetics and Mechanism for Formation of Enols in Reaction of Hydroxide Radical with Propene. *J. Phys. Chem. A* **2009**, *113*, 2372–2382.
- (35) Taatjes, C. A.; Hansen, N.; Miller, J. A.; Cool, T. A.; Wang, J.; Westmoreland, P. R.; Law, M. E.; Kasper, T.; Kohse-Hoinghaus, K. Combustion Chemistry of Enols: Possible Ethanol Precursors in Flames. *J. Phys. Chem. A* **2006**, *110*, 3254–3260.
- (36) Taatjes, C. A.; Hansen, N.; McLroy, A.; Miller, J. A.; Senosiain, J. P.; Klippenstein, S. J.; Qi, F.; Sheng, L.; Zhang, Y.; Cool, T. A.; Wang, J.; Westmoreland, P. R.; Law, M. E.; Kasper, T.; Kohse-Hoinghaus, K. Enols are Common Intermediates in Hydrocarbon Oxidation. *Science* **2005**, *308*, 1887–1889.
- (37) Cvetanovic, R. J. Chemical Kinetic Studies of Atmospheric Interest. *12th International Symposium on Free Radicals*, Jan. 4–9, 1976, Laguna Beach, CA; unpublished report.
- (38) Loison, J.; Daranlot, J.; Bergeat, A.; Caralp, F.; Mereau, R.; Hickson, K. M. Gas-Phase Kinetics of Hydroxyl Radical Reactions with C_3H_6 and C_4H_8 : Product Branching Ratios and OH Addition Site-Specificity. *J. Phys. Chem. A* **2010**, *114*, 13326–13336.
- (39) Feltham, E. J.; Almond, M. J.; Marston, G.; Wiltshire, K. S.; Goldberg, N. Reactions of Hydroxyl Radicals with Alkenes in Low-Temperature Matrices. *Spectrochim. Acta, Part A* **2000**, *56*, 2589–2603.
- (40) Izsak, R.; Szori, M.; Knowles, P. J.; Viskolcz, B. High Accuracy Ab Initio Calculations on Reactions of OH with 1-Alkenes. The Case of Propene. *J. Chem. Theory Comput.* **2009**, *5*, 2313–2321.
- (41) El-Nahas, A. M.; Uchimaru, T.; Sugie, M.; Tokuhashi, K.; Sekiya, A. A Relative Reactivity and Regioselectivity of Halogen-Substituted Ethenes and Propene toward Addition of and OH Radical or $O(^3P)$ Atom: An Ab Initio Study. *J. Mol. Struct.: THEOCHEM* **2006**, *770*, 59–65.
- (42) Ratliff, B. J.; Womack, C. C.; Tang, X. N.; Landau, W. M.; Butler, L. J.; Szpunar, D. E. Modeling the Rovibrationally Excited C_2H_4OH Radicals from the Photodissociation of 2-Bromoethanol at 193 nm. *J. Phys. Chem. A* **2010**, *114*, 4934–4945.
- (43) Womack, C. C.; Ratliff, B. J.; Butler, L. J.; Lee, S.-H.; Lin, J. J. Photoproduct Channels from $BrCD_2CD_2OH$ at 193 nm and the HDO + Vinyl Products from the CD_2CD_2OH Radical Intermediate. *J. Phys. Chem. A* **2012**, *116*, 6394–6407.
- (44) McKown, B. G.; Ceriotti, M.; Womack, C. C.; Kamarchik, E.; Butler, L. J.; Bowman, J. M. Effects of High Angular Momentum on the Unimolecular Dissociation of CD_2CD_2OH : Theory and Comparisons with Experiment. *J. Phys. Chem. A* **2013**, *117*, 10951–10963.
- (45) Heck, A. J. R.; Chandler, D. W. Imaging Techniques for the Study of Chemical Reaction Dynamics. *Annu. Rev. Phys. Chem.* **1995**, *46*, 335–372.
- (46) Eppink, A. T. J. B.; Parker, D. H. Velocity Map Imaging of Ions and Electrons Using Electrostatic Lenses: Application in Photoelectron and Photofragment Ion Imaging of Molecular Oxygen. *Rev. Sci. Instrum.* **1997**, *68*, 3477–3484.
- (47) Sato, Y.; Matsumi, Y.; Kawasaki, M.; Tsukiyama, K.; Bersohn, R. J. Ion Imaging of the Photodissociation of OCS Near 217 and 230 nm. *J. Phys. Chem.* **1995**, *99*, 16307–16314.
- (48) Liu, Y.; Butler, L. J. C-Cl Bond Fission Dynamics and Angular Momentum Recoupling in the 235 nm Photodissociation of Propionyl Chloride and the Barrier to Dissociation of the Propionyl Radical. *J. Chem. Phys.* **2004**, *121*, 11016–11022.

- (49) Chang, B.; Hoetzlein, R. C.; Mueller, J. A.; Geiser, J. D.; Houston, P. L. Improved 2D Product Imaging: the Real-Time Ion-Counting Method. *Rev. Sci. Instrum.* **1998**, *69*, 1665–1670.
- (50) Ratliff, B. J.; Alligood, B. W.; Butler, L. J.; Lee, S. -H.; Lin, J. J. -M. Product Branching from the $\text{CH}_2\text{CH}_2\text{OH}$ Radical Intermediate of the $\text{OH} + \text{Ethene}$ Reaction. *J. Phys. Chem. A* **2011**, *115*, 9097–9110.
- (51) Lin, J. J.; Chen, Y.; Lee, Y. Y.; Lee, Y. T.; Yang, X. Photodissociation Dynamics of CH_3Cl at 157.6 nm: Evidence for CH_2 (X^3B_1/a^1A_1) + HCl Product Channels. *J. Chem. Phys. Lett.* **2002**, *361*, 374–382.
- (52) Lee, S. -H.; Lee, Y. -Y.; Lee, Y. T.; Yang, X. Photodissociation Dynamics of Propene at 157.6 nm: Kinetic Energy Distributions and Branching Ratios. *J. Chem. Phys.* **2003**, *119*, 827–838.
- (53) Frisch, M. J.; Trucks, G. W.; Schlegel, H. B.; et al. *Gaussian 09*, Revision A.02; Gaussian, Inc.: Wallingford, CT, 2009.
- (54) Curtiss, L. A.; Redfern, P. C.; Raghavachari, K.; Pople, J. A. Gaussian-3X (G3X) Theory: Use of Improved Geometries, Zero-Point Energies, and Hartree-Fock Basis Sets. *J. Chem. Phys.* **2001**, *114*, 108–117.
- (55) Curtiss, L. A.; Redfern, P. C.; Raghavachari, K. Gaussian-4 Theory. *J. Chem. Phys.* **2007**, *126*, 084108.
- (56) Dribinski, V.; Ossadtchi, A.; Mandelshtam, V. A.; Reisler, H. Reconstruction of Abel-Transformable Images: The Gaussian Basis-Set Expansion Abel Transform Method. *Rev. Sci. Instrum.* **2002**, *73*, 2634–2642.
- (57) Womack, C. C.; Booth, R. S.; Brynteson, M. D.; Butler, L. J.; Szpunar, D. E. Rovibrational Distribution of $\text{CD}_2\text{CD}_2\text{OH}$ Radicals Produced via the Photodissociation of 2-Bromoethanol- d_4 . *J. Phys. Chem. A* **2011**, *115*, 14559–14569.
- (58) Van Veen, G. N. A.; Baller, T.; De Vries, A. E. Photo-fragmentation of CH_3Br in the A Band. *Chem. Phys.* **1984**, *92*, 59–65.
- (59) Alligood, B. W.; Straus, D. B.; Butler, L. J. Analyzing Velocity Map Images to Distinguish the Primary Methyl Photofragments from those Produced upon C-Cl Bond Photofission in Chloroacetone at 193 nm. *J. Chem. Phys.* **2011**, *135*, 034302.
- (60) Brynteson, M. D.; Butler, L. J. Manuscript in preparation, 2014.
- (61) Chhantyal-Pun, R.; Kline, N. D.; Thomas, P. S.; Miller, T. A. Observation of the A-X Electronic Transition of the β -Hydroxyethylperoxy Radical. *J. Phys. Chem. Lett.* **2010**, *1*, 1846–1852.
- (62) Edwards, L. W.; Ryazanov, M.; Reisler, H.; Klippenstein, S. J. D-Atom Products in Predissociation of $\text{CD}_2\text{CD}_2\text{OH}$ from 202 – 215 nm Photodissociation of 2-Bromoethanol. *J. Phys. Chem. A* **2010**, *114*, 5453–5461.
- (63) Womack, C. C.; Ratliff, B. J.; Butler, L. J.; Lee, S. -H.; Lin, J. J. Photoproduct Channels from $\text{BrCD}_2\text{CD}_2\text{OH}$ at 193 nm and the $\text{HDO} + \text{Vinyl}$ Products from the $\text{CD}_2\text{CD}_2\text{OH}$ Radical Intermediate. *J. Phys. Chem. A* **2012**, *116*, 6394–6407.